

Investigating episodic mass loss in evolved massive stars

III. Spectroscopy of dusty massive stars in three northern galaxies

S. de Wit^{1,★}, G. Muñoz-Sánchez^{1,2,★,★}, G. Maravelias^{1,3}, A. Z. Bonanos¹, K. Antoniadis^{1,2},
D. García-Álvarez^{4,5}, N. Britavskiy^{6,7}, A. Ruiz¹, and A. Philippopoulos⁸

¹ IAASARS, National Observatory of Athens, I. Metaxa & Vas. Pavlou St., 15236 Penteli, Athens, Greece

² Department of Physics, National and Kapodistrian University of Athens, Panepistimiopolis, Zografos 15784, Greece

³ Institute of Astrophysics, FORTH, 71110 Heraklion, Greece

⁴ Instituto de Astrofísica de Canarias, Avenida Vía Láctea, 38205 La Laguna, Tenerife, Spain

⁵ Grantecan S. A., Centro de Astrofísica de La Palma, Cuesta de San José, 38712 Breña Baja, La Palma, Spain

⁶ Royal Observatory of Belgium, Avenue Circulaire, Ringlaan 3, 1180 Brussels, Belgium

⁷ University of Liège, Allée du 6 Août 19c (B5C), 4000 Sart Tilman, Liège, Belgium

⁸ Department of Physics, University of Oxford, Oxford, UK

Received 20 December 2024 / Accepted 22 April 2025

ABSTRACT

Mass loss in massive stars is crucial to understanding how these stars evolve and explode. Despite increasing evidence of its importance, episodic mass loss remains poorly understood. Here we report the results of an optical spectroscopic survey of evolved massive stars in NGC 6822, IC 10, and IC 1613 conducted as part of the ASSESS project (Episodic Mass Loss in Evolved Massive Stars: Key to Understanding the Explosive Early Universe), which investigated the role of episodic mass loss by targeting stars with infrared excesses indicating a dusty circumstellar environment. We assigned a spectral class to 122 unique sources, the majority of which are dusty. The rate of evolved massive stars was over 60% for the highest-priority targets. We discovered two blue supergiants, one yellow supergiant, and one emission-line object, and confirmed two supernova remnant candidates, a Wolf–Rayet star, and two H II regions. Twenty-eight unique sources were classified as red supergiants (RSGs), 21 of which are new discoveries. In IC 10, we increased the sample of spectroscopically confirmed RSGs from 1 to 17. We used the MARCS models to obtain their surface properties, most importantly the effective temperature, and used spectral energy distribution fitting to obtain the stellar luminosity for 17 of them. The dusty RSGs are cooler, more luminous, more extinguished, and more evolved than the non-dusty ones, in agreement with previous findings. By investigating the optical photometric variability of the RSGs from light curves that cover a period of over a decade, we found that the dusty RSGs are more variable. We further highlight a very extinguished emission-line object, two RSGs that display a significant change in spectral type between two observed epochs, and four dusty K-type RSGs that may have undergone episodic mass loss.

Key words. catalogs – circumstellar matter – stars: evolution – stars: massive – stars: mass-loss – supergiants

1. Introduction

Massive stars lose a significant fraction of their mass as they evolve. For stars between 8 and 30 M_{\odot} , mass is gradually lost through stationary, line-driven winds in the OB phase (e.g., Castor et al. 1975; Vink et al. 2000; Vink & Sander 2021) and through stronger winds during the red supergiant (RSG) phase (e.g., de Jager et al. 1988; van Loon et al. 2005; Beasor et al. 2020; Yang et al. 2023; Antoniadis et al. 2024). The evolution of such stars (e.g., whether they transition to yellow hypergiants; Yoon & Cantiello 2010; Koumpia et al. 2020; Humphreys et al. 2023), their supernova explosion characteristics (Smartt et al. 2009; Smartt 2015; Förster et al. 2018), and the properties of the resulting compact object (Sukhbold et al. 2016; Vink & Sander 2021) are all affected by the degree of mass loss.

Reductions in the observed mass-loss rates in both the OB phase (Fullerton et al. 2006; Cohen et al. 2014; Telford et al. 2024) and the RSG phase (Beasor et al. 2020; Antoniadis et al. 2024; Decin et al. 2024) suggest that mass lost through

stationary winds is inadequate to strip stars of their hydrogen-rich envelopes. Evidence of episodic mass loss (Smith 2014) is mounting from theory (e.g., Cheng et al. 2024) and direct observations of massive stars (e.g., Ohnaka et al. 2008; Gvaramadze et al. 2010; Montargès et al. 2021; Muñoz-Sánchez et al. 2024a), superluminous supernovae (Gal-Yam 2012; Neill et al. 2011; Gal-Yam 2019), and supernova “impostors” (e.g., SN2009ip; Mauerhan et al. 2013; Smith et al. 2022).

Hints of ongoing or recent epochs of enhanced mass loss in RSGs may lie in their circumstellar environments (Ohnaka et al. 2008; Montargès et al. 2021; Dupree et al. 2022; Decin et al. 2024). The presence of infrared (IR) excesses due to recent dust formation provides a laboratory to study mass-losing RSGs with increased surface activity (Ma et al. 2024; Drevon et al. 2024). Pulsations (Yoon & Cantiello 2010), convective cycles (Josselin & Plez 2007; Kravchenko et al. 2019), radiation pressure on molecules (Arroyo-Torres et al. 2015), and turbulence (Josselin & Plez 2007; Kee et al. 2021) are all thought to contribute to the surface conditions that enable mass loss. Therefore, the large-scale characterization of RSG surfaces is crucial to understanding which RSGs have the conditions for episodic mass loss and how frequent these episodes are. The latter has implications

* These authors contributed equally and should be considered joint first authors.

** Corresponding author.

Table 1. Properties of the target galaxies.

Galaxy	RA (J2000)	Dec (J2000)	Distance (Mpc)	Diameter ($''$)	12+ log(O/H) ^(a)	Z (Z _⊙)
IC 10	00:20:23.11	+59:17:35.2	0.77 ^{+0.01} _{-0.02} (1)	7	8.37 ⁽²⁾	0.30 ⁽³⁾
IC 1613	01:04:47.78	+02:07:03.7	0.74 ^{+0.03} _{-0.05} (4)	18	7.62 ⁽⁵⁾	0.20 ⁽⁶⁾
NGC 6822	19:44:56.98	-14:48:01.1	0.48±0.03 ⁽⁷⁾ , 0.45 ^{+0.01} _{-0.02} (8)	19	8.14 ⁽⁹⁾	0.30 ⁽¹⁰⁾

Notes. ^(a) 12+ log(O/H)_⊙ = 8.75 (Bergemann et al. 2021). (1) McQuinn et al. (2017), (2) Cosens et al. (2024), (3) Polles et al. (2019), (4) Górski et al. (2011), (5) Lee et al. (2003), (6) Bresolin et al. (2007), (7) Tully et al. (2013), (8) Zgirski et al. (2021), (9) Moustakas et al. (2010), (10) Patrick et al. (2015).

for the duration of such a phase, whereas the surface properties may be linked to the stage of the RSG evolution during which this occurs.

The ASSESS project¹ (Episodic Mass Loss in Evolved Massive Stars: Key to Understanding the Explosive Early Universe) has so far observed and classified 185 evolved massive stars (Bonanos et al. 2024) and modeled 127 RSGs (de Wit et al. 2024) to obtain their properties. Additionally, the project has conducted spectroscopic and photometric variability studies of extreme RSGs such as [W60] B90 and WOH G64 (Munoz-Sanchez et al. 2024a,b, respectively) to understand their variable nature and the connection to episodic mass loss. This paper aims to increase the number of classified evolved massive stars, from which the classified RSGs are modeled, by presenting and analyzing spectra from three galaxies in our northern survey: NGC 6822, IC 10, and IC 1613. Section 2 presents the target selection, observations, and data reduction. Section 3 provides the spectral classification for each object and the catalog. Section 4 presents RSG luminosities, optical light curves, and the RSG properties determined from modeling, and we discuss them in Sect. 5. Section 6 summarizes our findings.

2. Observations and data reduction

2.1. Target selection

Table 1 presents the properties of the target galaxies (i.e., IC 10, IC 1613, and NGC 6822), such as coordinates, distance, diameter (i.e., the size of the galaxy based on visual inspection) used to match the catalogs, the oxygen abundance log(O/H), and metallicity Z. For NGC 6822, we built the catalog and selected the targets using the CosmicFlows-2 distance of 0.48 Mpc (Tully et al. 2013). An updated distance (0.45 ± 0.01 Mpc; Zgirski et al. 2021) was published after our observations; hence, we used it in the analysis (see Sect. 4). We selected targets using multiwavelength photometric catalogs. We began with *Spitzer* IR catalogs from Khan et al. (2015) for NGC 6822 and Boyer et al. (2015) for IC 10 and IC 1613. We cross-matched them using a 1 $''$ radius with *Gaia* astrometry (Gaia Collaboration 2016, 2018), optical photometry (Pan-STARRS1; Chambers et al. 2016), and near-IR photometry. For the near-IR photometry, we used the UK Infra-Red Telescope Hemisphere Survey (Dye et al. 2018; Irwin 2013) for IC 10 and the VISTA Hemisphere Survey (McMahon 2012) for NGC 6822. No data were available for IC 1613. We used the photometric datasets for the target selection and *Gaia* to identify and remove foreground sources.

We applied the criteria presented by Bonanos et al. (2024), which rely on early road maps from Bonanos et al. (2009, 2010)

showing the separation of classes of evolved massive stars based on their mid-IR colors. First, we considered sources with $[3.6] - [4.5] \geq 0.1$ mag, corresponding to dusty sources and excluding foreground stars (see, e.g., Britavskiy et al. 2015). Then, cuts in the absolute magnitude $M_{3.6} \leq -9.0$ mag and the apparent magnitude of $[4.5] \leq 15.5$ mag were applied to exclude contamination from the asymptotic giant branch (AGB) stars and background sources (such as galaxies and quasars), respectively. We assigned a priority scheme (from P1 to P6) depending on the mid-IR color, absolute magnitude criteria, and the presence of optical or near-IR counterparts (see Bonanos et al. 2024 for details). The highest priority candidates, P1 and P2, correspond to the brightest IR sources with strong and moderate IR excess, respectively. Table A.1 presents the distribution of priorities for all the available targets, as well as for the observed targets in each field of multi-object spectroscopy (MOS) and long-slit observation. Overall, we observed 97 priority targets: 42 targets in IC 10 (34% of the total available priority targets), 3 targets in IC 1613 (18% of the total), and 52 targets in NGC 6822 (54% of the total). We had a notable coverage of the highest-priority classes, with 9 P1 and 5 P2 targets (60% and 71% of the total, respectively).

2.2. Pre-imaging and mask design (MOS)

We obtained the spectra for a large number of targets with the MOS mode of the Optical System for Imaging and low-Intermediate-Resolution Integrated Spectroscopy (OSIRIS; Cepa et al. 2000, 2003) at the 10.4 m Gran Telescopio Canarias (GTC), at La Palma, Canary Islands.

During our first observing campaign (proposal ID 115-GTC83/20A, PI: N. Britavskiy) MOS observations were carried out for IC 10 and NGC 6822. We first acquired short exposures (10–15 s in the *r* filter) of the fields to be observed. This pre-imaging, combined with the Mask Designer tool (v. 3.26²), helped us securely identify targets in the field of view and design the mask (i.e., the positions of the slits). We used the 1000R grism and a 1.2 $''$ slit width, which yielded a spectral resolving power ($R = \lambda/\Delta\lambda$) of ~600–1000, depending on the seeing (see Table A.2), over the wavelength range of ~5300–9000 Å. The resolution and wavelength coverage provide access to a large number of spectral features critical for spectral classification (see Sect. 3). Targets at the edges of the detector yield a more limited spectral range. The pointings were chosen to maximize the number of P1 and P2 targets to be observed. Additional space on each mask was filled with lower-priority targets.

For the second campaign (proposal ID 29-GTC34/22A, PI: D. García-Álvarez), the MOS observing mode was not available.

² https://www.gtc.iac.es/instruments/osiris/osirisMOS_Cass.php#MDtool

¹ <http://assess.astro.noa.gr/>

Table 2. Distribution of classified targets per galaxy and spectral class.

Galaxy name	Class.	RSG	BSG	YSG	C-stars	H II	Em. Obj.	Fgd	Other ^(a) stars	Clusters	Galaxies	SNR
IC 10	46 (12)	6 (10)	1	–	6 (2)	–	–	17	11	2	–	3
IC 1613	3 (3)	1 (1)	– (1)	– (1)	–	–	–	1	–	–	1	–
NGC 6822	36 (7)	7 (3)	–	–	7 (2)	2	1	3	15 (2)	1	–	–
Total	85 (22)	14 (14)	1 (1)	0 (1)	13 (4)	2	1	21	26 (2)	3	1	3

Notes. The parentheses indicate the number of candidate sources per spectral class. ^(a)Other A, F, G, M stars, hot, warm, cool stars, and the WC star are grouped into “Other stars.”

However, we were able to secure several long-slit observations for a selection of targets in IC 10, IC 1613, and NGC 6822. For these, we used the 1000R grism and a 0.8'' slit width, achieving $R \sim 1000$. Whenever possible, we placed two targets in the slit. In all cases, we used the standard bias, flat-field, and arc exposures provided by the observatory.

Table A.2 presents the observing log for all OSIRIS pre-imaging, MOS, and long-slit observations, providing the coordinates of the field center for MOS spectra or of the target for long-slit spectra, the UT date, modified Julian date, mode, exposure time, airmass, and seeing for each observation.

2.3. Data reduction

We performed the data reduction of the MOS observations in two steps. First, we used the GTCMOS package (an IRAF³ based pipeline, Gómez-González et al. 2016) to merge the images from each CCD⁴ and subtract the bias. Due to an offset between the flat field and the science images, which compromised the sky subtraction process in the narrow slits by creating artifacts close to the edges of the slits, we discarded the flat correction. We therefore proceeded to manually reduce the spectra using the IRAF tasks IDENTIFY, REIDENTIFY, FITCOORDS, and TRANSFORM to get a 2D-wavelength calibrated image, and APALL to extract the spectra. We flux-calibrated the extracted spectra with the flux standard by using the tasks STANDARD, SENSFUNC, and CALIBRATE. We followed the same manual approach to reduce the long-slit spectra. For both the MOS and long-slit observations, serendipitous extracted stars, which do not fall into any priority category, are labeled “R” (i.e., random) in Table A.1 (e.g., IC10-R1). We computed and applied the heliocentric correction with RVCORRECT.

3. Spectral classification and stellar content

Out of the 163 spectra, we classified 124 into broad classes, following the procedure and criteria described by Bonanos et al. (2024). The other 39 spectra could not be classified due to their low S/N. Two sources were reobserved (IC10-5660 and IC10-9165) with the OSIRIS long-slit mode due to their apparent brightness and late RSG type (see Sect. 3.1), yielding 122 unique sources classified. 15 targets out of the 122 were classified more generally, like a nebula or a red source. Table 2 presents the

distribution of classified targets (107) for both robust classifications (85) and candidates (22) per galaxy and spectral class. Figure 1 shows the spatial distribution of the H II regions, carbon stars, and evolved massive stars and Fig. 2 their location in the color-magnitude diagrams. Note, particularly in IC 10, that the absolute magnitudes M_G and $M_{3.6}$ are not corrected for foreground extinction ($A_V = 4.3$ mag, Schlafly & Finkbeiner 2011).

Table 3 presents the catalog, including all 122 spectroscopically classified targets. The targets are sorted by galaxy name and the ID, which is based on [4.5] (see Bonanos et al. 2024, for a description). The columns of Table 3 indicate the J2000 coordinates (in degrees), the observed field, assigned priority, *Gaia* DR3 photometry, *Gaia* DR3 astrometry (Gaia Collaboration 2023), *Spitzer* photometry (Fazio et al. 2004; Rieke et al. 2004), Pan-STARRS1 DR2 photometry (Chambers et al. 2016), UKIRT Hemisphere Survey photometry (Dye et al. 2018), the VISTA Hemisphere Survey photometry (McMahon 2012, NGC 6822 only), median absolute deviations (MAD; see Sect. 4.2), spectral type, previous classifications from the literature and comments on the spectral classification of each source. Previous classifications from the literature were obtained by cross-matching our sources using the Vizier catalog access tool and a 1'' radius. The catalog includes 21 newly discovered RSGs and 4 other evolved massive stars.

3.1. RSG classification

We classified the RSGs more precisely than the other classes following the classification criteria by de Wit et al. (2024). In addition to those criteria, if a strong Ca II triplet was observed and its radial velocity corresponded to that of the host galaxy, the sources were robustly classified as RSGs. We securely classified 14 targets as RSGs and verified that their modeled properties agreed with the expected range of properties for RSGs in these galaxies. However, we added a colon after the luminosity indicator (e.g., K5–M0 I:) when the S/N was low at the Ca II triplet or at least one modeled property was outside the expected range (e.g., their surface gravity was too high, or the recovered $E(B - V)$ too low, in the case of IC 10). We considered the other 14 RSGs as candidates, given that oxygen-rich AGB stars are likely contaminants (reaching up to $\log(L/L_\odot) \sim 5.0$, but with weaker Ca II lines; Groenewegen & Sloan 2018).

The 28 verified and candidate RSGs include sixteen in IC 10, two in IC 1613, and ten in NGC 6822. We classified them as: one GK I, two K0–K5 I, three K5–M0 I, fourteen M0–M2 I, six M2–M4 I, and four M4–M6 I (see some examples in Fig. 3). The criteria for the M4–M6 I class were not presented by de Wit et al. (2024) as their spectra did not cover the TiO band

³ IRAF is distributed by the National Optical Astronomy Observatory, operated by the Association of Universities for Research in Astronomy (AURA) under agreement with the National Science Foundation.

⁴ For observations taken in 2020, while the 2022 upgrade implemented a monolithic CCD.

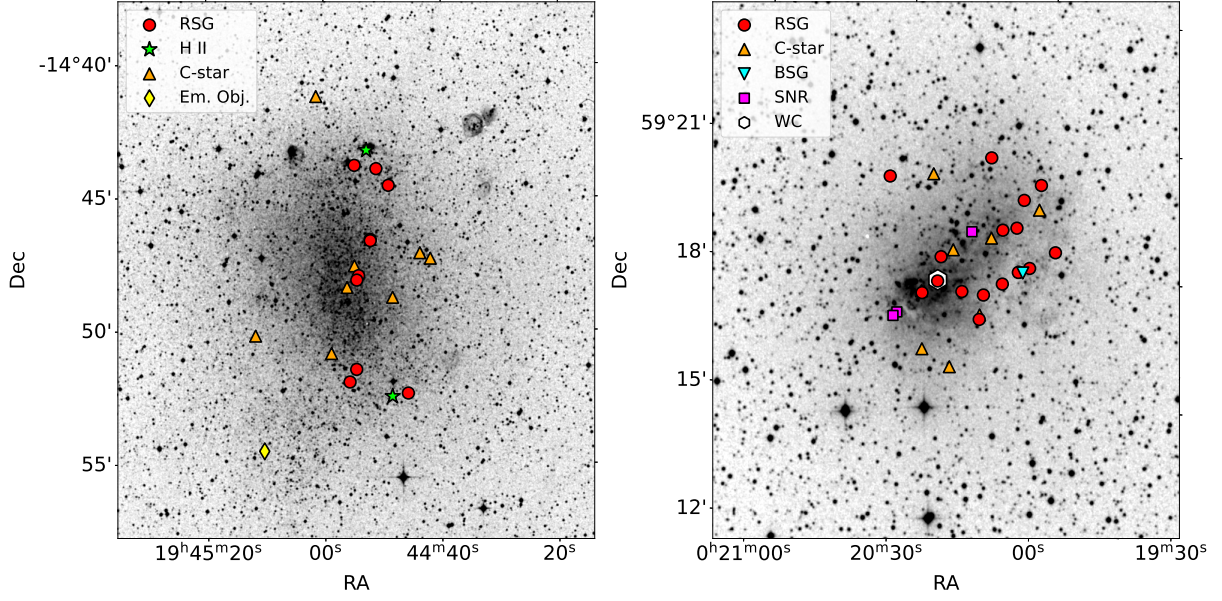


Fig. 1. Spatial distribution of classified sources in NGC 6822 (left) and IC 10 (right); background images are from DSS2-red.

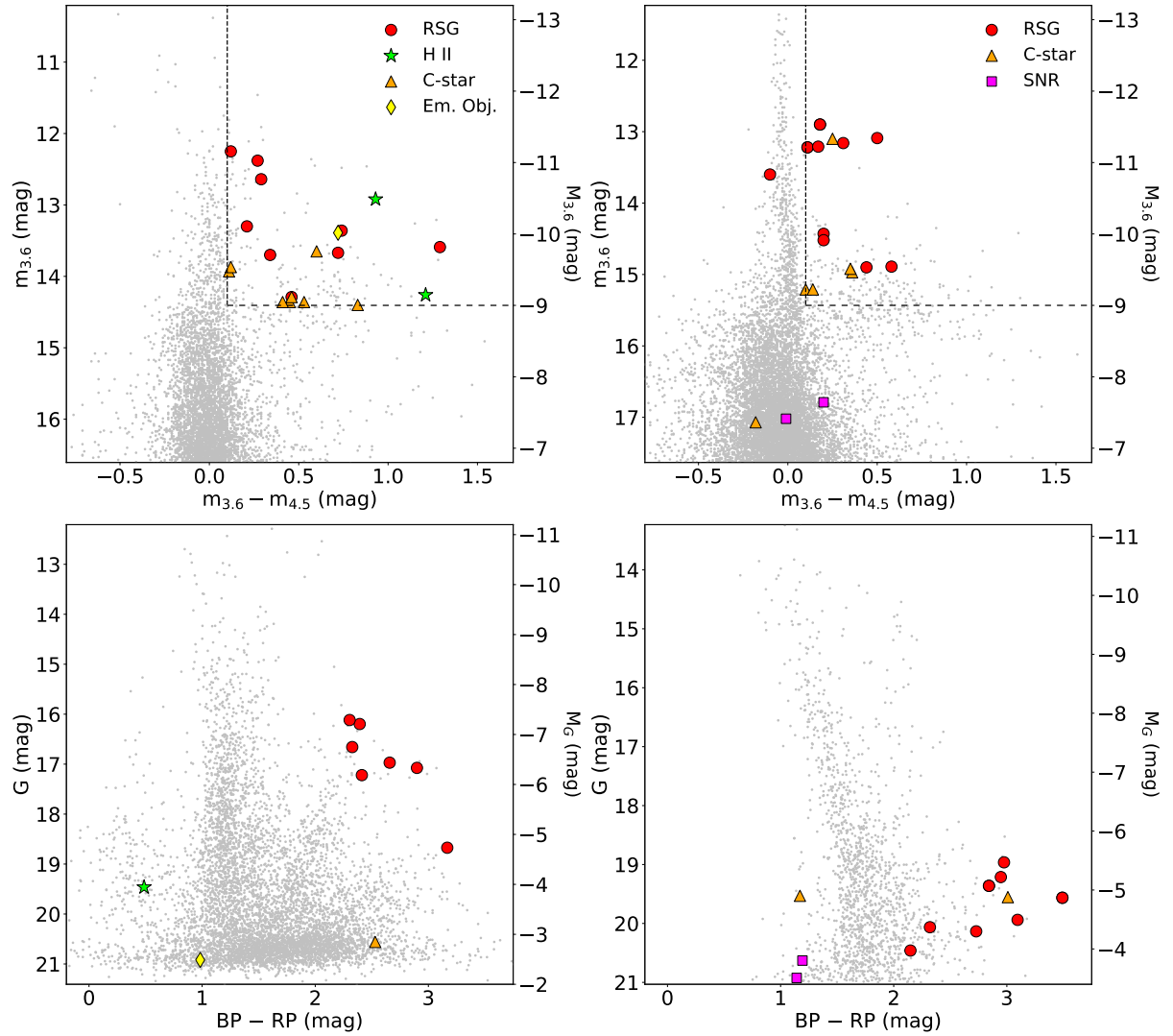


Fig. 2. Near-IR and optical color-magnitude diagrams of classified sources. We show the locations of classified targets with *Spitzer* IRAC photometry for NGC 6822 (top left) and IC 10 (top right) and with *Gaia* photometry for NGC 6822 (bottom left) and IC 10 (bottom right). The dashed lines indicate the priority criteria from Bonanos et al. (2024). IC10-52406 is the only RSG that shows no IR excess, as it was a serendipitous observation.

Table 3. Spectral classifications.

ID	RA	Dec	...	Spectral Class.	Classification notes
IC10-5545	5.09071	59.30489	...	K0–K5 I	Weak TiO abs. Strong Ca II triplet.
IC10-5660	5.10571	59.29033	...	M4–M6 I: & M0–M2 I:	Strong TiO abs (TiO λ 8430 present). Strong Ca II triplet. Neb em lines.
IC10-6884	5.09643	59.29376	...	AF-star	Lack of spectral lines. Ca II λ 8542 abs.
IC10-7387	5.10304	59.26844	...	C-star	CN band abs.
IC10-8523	5.10129	59.33703	...	C-star	CN band abs.
IC10-9165	5.09258	59.29533	...	M4–M6 I: & M0–M2 I	Strong TiO abs (TiO λ 8430 present). Strong Ca II triplet.
IC10-10128	5.05371	59.29040	...	K V	Strong D1/D2 abs. Weak Ca II triplet.
IC10-11499	4.93359	59.32721	...	AFG V	Strong H α abs. Strong metal abs.
IC10-16046	5.05946	59.28856	...	Red	
IC10-16200	5.05233	59.34828	...	Red	Unidentified molecular abs around λ 7000
IC10-17332	5.03544	59.29600	...	M V	TiO abs.
IC10-17517	5.02783	59.32278	...	Composite:	Multiple stellar contributions
IC10-18665	5.07206	59.30387	...	AFG V	Weak H α . Ca II triplet present.
IC10-19636	5.03346	59.25064	...	M-star	TiO abs.
IC10-20273	5.07797	59.31839	...	AFG V	Strong H α abs. Strong metal abs.

Notes. This table is available in its entirety at the CDS. A portion is shown here for guidance regarding its form and content.

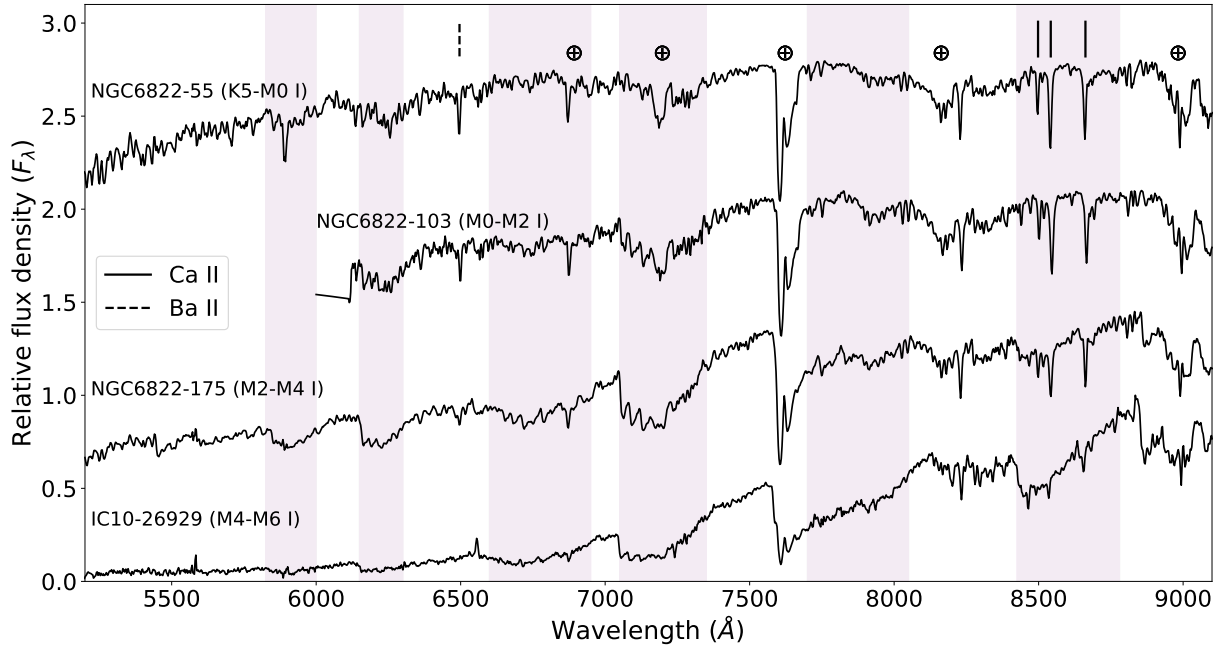


Fig. 3. OSIRIS spectra of classified RSGs. We show four RSGs with increasing TiO absorption strengths, which highlights the spectral type sequence of RSGs. Purple-shaded areas indicate regions with TiO absorption. A \oplus marks telluric absorption.

starting around λ 8430. Typically, when this TiO band dominates the absorption in the *I* band, stars are classified with spectral types ranging from M4 to M6 (Solf 1978). The targets classified twice (IC10-5660 and IC10-9165) shifted from M4–M6 I in their MOS spectrum (August 2020) to M0–M2 in their long-slit spectrum (August 2022), significantly changing their TiO band strengths. The GK I supergiant (IC1613-28306) lacks TiO bands, and the “forest” of metallic lines from λ 5500–6500 indicated a slightly hotter source, bordering the yellow supergiant (YSG) class. However, some individual spectral lines (e.g., H α) are too strong for such a star, hinting at a potential binary component. These spectra are modeled for their stellar properties in Sect. 4.3.

We find the average spectral type of the sample to be M0–M2 I, which agrees with that expected at $Z \sim 0.3$ (Levesque & Massey 2012) and increases the sample at this metallicity. The metallicity dependence of the average spectral type, and, subsequently, of the effective temperature, was first reported by Elias et al. (1985) and is due to the shift of the Hayashi limit to higher temperatures at low metallicities. The small fraction of K-type RSGs (21%) can also be attributed to the absolute magnitude selection criteria, as we mainly targeted bright RSGs. These are more likely to exhibit higher mass loss rates, increasing the TiO band strengths and shifting the RSGs to later types (Davies & Plez 2021).

Seven out of the 28 RSGs were previously reported in the literature: IC1613-28306, NGC 6822-52, NGC 6822-55, NGC 6822-66, NGC 6822-70, NGC 6822-103, and NGC 6822-175 (Massey 1998; Massey et al. 2007; Levesque & Massey 2012; Patrick et al. 2015; Chun et al. 2022). IC10-66828 is located in a known cluster (Tikhonov & Galazutdinova 2009). Kacharov et al. (2012) classified NGC 6822-248 as an M6 III star, but they only distinguished between foreground (V) and giant (III) stars; hence, our classification supersedes it. Finally, only one spectroscopically confirmed RSG was previously known in IC 10 (Britavskiy et al. 2019); therefore, by adding 16 RSGs, our work has significantly increased the RSG sample in this galaxy.

3.2. Other sources

We identified two blue supergiants (BSGs) and a YSG in the sample (see Fig. B.1): IC1613-8006 (A I–III), IC1613-6612 (AFG I–III), and IC10-21061 (BA I). The Paschen absorption series in the spectra of IC1613-8006 and IC10-21061 indicated a spectral type A. In contrast, metal lines in the spectrum of IC1613-6612 suggested a cooler, YSG candidate. The slope of IC10-21061 was severely reddened due to the foreground extinction, but its significantly blue-shifted $H\alpha$ emission line profile supported the extragalactic supergiant classification. Additionally, we classified IC10-R15 as a Wolf–Rayet star based on the strong C IV feature at 5800 Å, which agrees with the previous classification from (Crowther et al. 2003).

We classified 17 carbon stars in our sample, of which 13 are robust classifications. Each of these exhibited strong CN absorption bands in the *R* and *I*-bands, occasionally displaying the Swan C₂ bands if the signal in the blue was high enough (see Fig. B.2; NGC 6822-170 and NGC 6822-387).

We classified three spectra as supernova remnants (SNRs) in IC 10. These spectra have emission lines (e.g., $H\alpha$, [S II], and [N II]) of nebular origin. The emission line ratios indicate a shock-ionization mechanism ([S II]/ $H\alpha \geq 0.4$), most commonly observed in SNRs (Kopsacheili et al. 2020). IC10-R23 matches the location of the radio source [YS93] HL20b (Yang & Skillman 1993), a known SNR. The other two are located where other SNR candidates have been reported from radio observations (Yang & Skillman 1993); hence, our optical spectra confirm their nature.

Figure B.3 plots the H II regions and Fig. B.4 the emission line object NGC 6822-106. The latter shows strong emission features but differs from those observed in the H II regions (e.g., [Ar III] and He I lines are absent, Ca II triplet in emission). NGC 6822-48 is a well-studied extended H II region (Hubble V; Hubble 1925; Rubin et al. 2016), hosting an O-star in the center with visible He II absorption lines (i.e., He II $\lambda 5412$), while NGC 6822-169 is a known compact H II region (Region γ ; Kinman et al. 1979).

3.3. High-priority sources

We highlight the highest-priority classified targets (P1 and P2), potentially very dusty evolved massive stars, which occupy the reddest region of Fig. 2.

Three of the nine P1 targets could not be classified due to their low S/N. We found three RSGs, one K0–K5 I (IC10-26089) and two M0–M2 I (NGC 6822-66 and NGC 6822-103), an H II region (NGC 6822-48), an emission line object (NGC 6822-106), and a star of spectral type M5–M9 (NGC 6822-77). Regarding NGC 6822-77, the lack of a visible Ca II triplet and its late spectral type suggest a foreground dwarf. We could not verify this with *Gaia* due to the absence of proper motion data.

From the five P2 targets, three were classified as cool RSGs (NGC 6822-70; M2–M4 I and NGC 6822-52 and IC10-26929; M4–M6 I), suggesting these are evolved, mass-losing RSGs (de Wit et al. 2024). The remaining two targets were classified as a carbon star (IC10-50206) and a cluster (NGC 6822-234), known as Hubble VII (Hubble 1925), which may contain a large amount of dust causing the apparent IR excess.

4. Properties of RSGs

4.1. SED fitting

We used the photometry presented in Table 3 to construct the spectral energy distribution (SED) of each RSG. We also added the median value of the time-series photometry from the *Zwicky* Transient Facility (ZTF; Bellm et al. 2019). Following the procedure described by de Wit et al. (2024), the magnitudes were corrected for foreground Galactic extinction from Schlafly & Finkbeiner (2011) in their respective bands. We fitted the observed SED with a Planck function to obtain the total observed flux. We adopted a distance of 0.77 ± 0.02 Mpc for IC 10 (McQuinn et al. 2017), 0.74 ± 0.03 Mpc for IC 1613 (Górski et al. 2011), and 0.45 ± 0.01 Mpc for NGC 6822 (Zgirski et al. 2021) to convert the observed flux into an intrinsic flux, yielding the bolometric luminosity. Table 4 presents the obtained luminosity, $\log(L/L_{\odot})$, of 17 RSGs through this SED fitting, and Fig. C.1 shows their fits. We could not obtain the luminosity for 11 RSGs because of the poor photometric coverage of their SED or contaminated photometry due to low spatial resolution.

None of the upper luminosity limits exceed or are even close to the observed upper luminosity limit of $\log(L/L_{\odot}) \sim 5.5$ for cool supergiants (Davies et al. 2018; McDonald et al. 2022). The two RSGs that show a large shift in their TiO band strengths (IC10-5660 and IC10-9165) have high $\log(L/L_{\odot}) \sim 5.3$, which indicates a very evolved state (Davies et al. 2013).

4.2. Light curves

We constructed light curves of the RSGs to search for correlations of variability with mass loss (e.g., Yang et al. 2018; Antoniadis et al. 2024). Optical multi-epoch photometry from *Gaia* DR3, ZTF, the Asteroid Terrestrial-impact Last Alert System (ATLAS; Tonry et al. 2018), and Pan-STARRS1 DR2 were collected; the ZTF and ATLAS data from the same night were binned by taking the median magnitude per night. Figure 4 presents the light curve of the well-sampled NGC 6822-55, while Fig. D.1 plots the light curves of the other 19 RSGs. Four targets in IC 10 are only well-sampled in the *izy* bands due to the high foreground extinction. The cadence provided by the ZTF light curves is sufficient to study their periodicity (see the analysis of seven targets by Christodoulou et al. 2025). Fig D.2 shows the transmission curves of each filter as a reference.

We computed the MAD of each RSG in the ZTF-*r*, ATLAS-*o*, and *G* bands (Table 3) and present the MAD versus magnitude in Fig. 5. To calculate the MAD, we require a target to have at least two measurements in one band, with an uncertainty of less than 0.1 mag. We considered a RSG as a certain variable when the MAD value is at least 1σ above the general distribution for a given magnitude. The most variable RSGs in our sample (NGC 6822-52, NGC 6822-55, and IC10-63627) are also among the most luminous ($\log(L/L_{\odot}) > 5.10$) and, therefore, are expected to have the highest mass-loss rates. For the two most luminous RSGs (IC10-5660 and IC10-9165), we are missing

Table 4. Stellar parameters of the RSG sample.

ID	Spectral Class.	S/N	Flags ^(a)	$T_{\text{eff,TiO}}$ (K)	$E(B - V)$ (mag)	$\log g$ (dex)	v_{rad} (km s ⁻¹)	$\log(L/L_{\odot})$ (dex)	R/R_{\odot}
NGC 6822-52	M4–M6 I:	61	1, 2	3350±50	0.30±0.01	0.98±0.01	−55±6	5.10±0.06	1050 ⁺¹¹⁰ _{−100}
NGC 6822-55	K5–M0 I	23	–	3960±50	0.20±0.02	0.2±0.2	−79±6	5.21±0.05	850±70
NGC 6822-66	M0–M2 I	54	–	3740±50	0.14±0.01	0.05±0.08	−79±3	5.19±0.05	940±80
NGC 6822-70	M2–M4 I	51	–	3510±50	0.24±0.01	0.06±0.09	−32±4	5.01±0.05	860 ⁺⁸⁰ _{−70}
NGC 6822-103	M0–M2 I	41	–	3680±50	0.16±0.01	−0.07±0.09	85±1	5.01±0.05	790 ⁺⁷⁰ _{−60}
NGC 6822-151	K5–M0 I:	69	4	3750±50	0.10±0.01	−0.44±0.04	−169±3	–	–
NGC 6822-175	M2–M4 I:	52	2	3530±50	0.19±0.01	0.8±0.1	−20±4	4.81±0.05	670±60
NGC 6822-248	M2–M4 I	46	–	3420±50	0.39±0.01	0.70±0.13	0±6	4.46±0.04	480±40
NGC 6822-407	M2–M4 I:	7	4	3510±50	0.12±0.05	0.7 ^{+0.2} _{−0.4}	56±23	–	–
NGC 6822-R10	M0–M2 I	14	–	3610±50	0.43±0.02	0.3±0.3	61±13	–	–
IC10-5545	K0–K5 I	14	–	4250±100	0.74±0.05	−0.3 ^{+0.2} _{−0.1}	−520±15	4.61±0.06	370 ⁺⁵⁰ _{−40}
IC10-5660A	M4–M6 I:	48	3	3450±50	0.45±0.01	0.4±0.1	−170±5	5.27±0.06	1210 ± 120
IC10-5660B ^(b)	M0–M2 I:	25	–	3530±50	0.44±0.02	0.5±0.2	−302±9	5.27±0.06	1160 ± 90
IC10-9165A	M4–M6 I:	53	3	3360±50	0.94±0.01	0.7±0.1	−140±6	5.26±0.03	1260 ± 80
IC10-9165B ^(b)	M0–M2 I	16	–	3510±50	1.31±0.04	0.5±0.3	−336±12	5.26±0.03	1150 ± 70
IC10-20296	M2–M4 I:	16	2, 4	3400±50	0.84±0.06	0.92 ^{+0.06} _{−0.14}	−455±21	4.13±0.07	330 ⁺⁴⁰ _{−30}
IC10-26089	K0–K5 I	36	–	4250±50	1.04±0.01	−0.44 ^{+0.07} _{−0.04}	−240±5	5.28±0.04	800±60
IC10-26929	M4–M6 I:	47	2,3	3330 ⁺⁵⁰ _{−30}	1.05±0.01	0.97 ^{+0.02} _{−0.05}	−181±8	–	–
IC10-35694 ^(b)	M0–M2 I	22	–	3530±50	0.67±0.02	0.2±0.2	−317±9	–	–
IC10-52406 ^(b)	M0–M2 I	18	–	3420±50	1.71±0.04	−0.1±0.2	−435±11	5.07±0.03	980 ⁺⁷⁰ _{−60}
IC10-63627 ^(b)	M0–M2 I	25	–	3650±50	0.83±0.02	0.2±0.2	−384±8	5.35±0.03	1180 ⁺⁸⁰ _{−70}
IC10-66828 ^(b)	M0–M2 I:	38	1,2	3670±50	0.10±0.01	0.96 ^{+0.03} _{−0.06}	−355±6	–	–
IC10-66981 ^(b)	M0–M2 I:	10	4	3550±50	0.69±0.04	0.4±0.4	−353±25	–	–
IC10-R3 ^(b)	M0–M2 I:	69	2	3630±50	0.23±0.01	1.00±0.01	−167±3	4.05±0.08	270±30
IC10-R10	M0–M2 I:	11	4	3480±50	0.85±0.05	0.4±0.4	−402 ⁺²⁷ _{−28}	–	–
IC10-R16	K5–M0 I:	9	4	3600±50	0.88±0.07	0.1±0.5	−390±40	–	–
IC10-R17	M2–M4 I:	18	4	3420±50	0.36±0.02	−0.43 ^{+0.10} _{−0.05}	−216±15	–	–
IC10-R20	M0–M2 I:	12	2, 4	3620±50	0.82±0.05	0.70±0.3	−480±30	–	–
IC1613-23465 ^(b)	M0–M2 I:	44	2, 4	3540±50	0.17±0.01	1.00±0.01	−244±5	4.35±0.09	400 ⁺⁶⁰ _{−50}
IC1613-28306 ^(b)	GK I	41	–	4380±50	0.09±0.01	0.23±0.09	−278±4	4.06±0.09	190 ⁺³⁰ _{−20}

Notes. Reported uncertainties are 68.3% confidence level errors. The v_{rad} of the MOS spectra have systematic uncertainties of ~ 60 km s⁻¹. The ending A/B in the ID indicates different observations of the same source. ^(a)Flags: (1) bad fit to spectrum, star too cool, parameters unreliable. (2) $\log g$ near the edge of the grid, lower limit. (3) acceptable fit, reliable parameters, but to be interpreted with caution. (4) bad fit to Ca II triplet, surface gravity unreliable. ^(b)Long-slit spectra. ^(c)The high S/N, high $\log g$, and low luminosity suggest a foreground nature for this star.

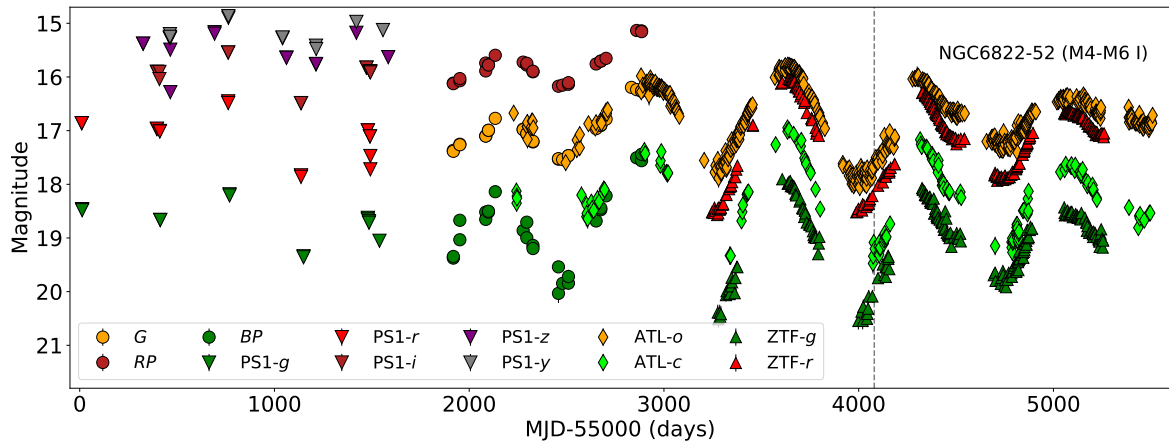


Fig. 4. Multi-survey optical light curve of NGC 6822-52. Apparent magnitudes from Pan-STARRS1 DR2 (triangles: *gri*), *Gaia* DR3 (circles: *G*, *BP*, *RP*), ZTF (upper triangles: *g*, *r*), and ATLAS (diamonds: *c*, *o*) are shown. The vertical dashed line indicates the epoch of the OSIRIS spectroscopy.

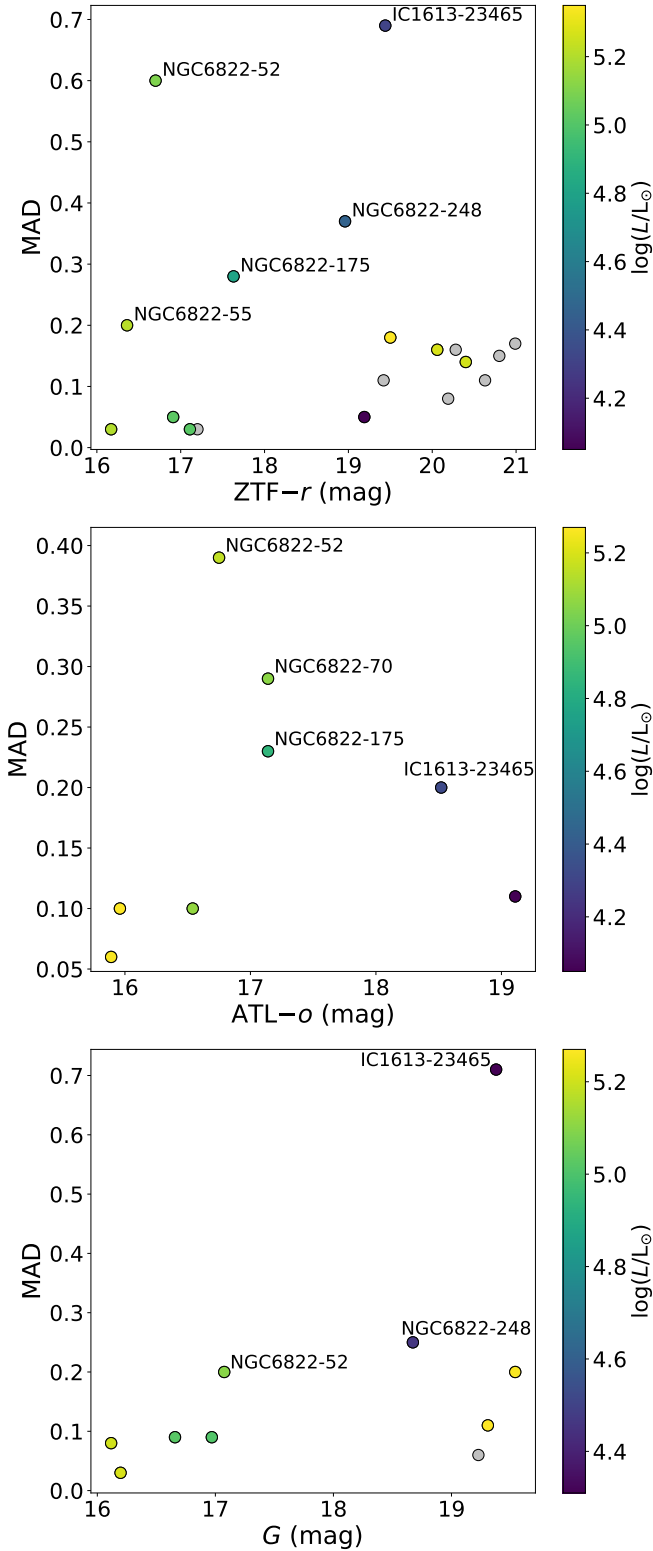


Fig. 5. MAD vs. magnitude diagram of RSGs in the ZTF-*r* (top), ATLAS-*o* (middle), and *Gaia*-*G* (bottom) bands. Variable RSGs with firm classifications are labeled.

either the coverage or high-quality photometry needed to properly assess their variability. Additionally, NGC 6822-175 exhibits high variability despite having a lower luminosity ($\log(L/L_{\odot}) = 4.80 \pm 0.05$). The low-mass RSGs (i.e., $10 M_{\odot}$) only reach $\log(L/L_{\odot}) \approx 5.0$; hence, NGC 6822-175 might be an evolved low-mass RSG, explaining its large variability. On the other

hand, we found extreme short-timescale variability – commonly seen in AGB stars – in two RSG candidates (NGC 6822-151 and IC 1613-23465) and the confirmed NGC 6822-248. We could not determine the luminosity of NGC 6822-151; the other two RSGs have low luminosities of $\log(L/L_{\odot}) < 4.50$, which is in the range where RSGs and massive AGB stars overlap (see Sect. 5.1 for more discussion).

4.3. Grid of models and the spectral fitting method

To obtain the properties of the RSGs, we fitted MARCS model atmospheres (Gustafsson et al. 2008) to our spectra. The wavelength range covers the Ca II (i.e., $\lambda 8498$, $\lambda 8542$, and $\lambda 8662$) triplet and multiple TiO bands (i.e., $\lambda 6150$, $\lambda 6650$, $\lambda 7050$, $\lambda 7700$, and $\lambda 8420$), constraining on the surface gravity ($\log g$) and effective temperature (T_{eff}), respectively. We used the spherical MARCS model grid presented by de Wit et al. (2024), ranging from 3300–4500 K and -0.5 to 1.0 for the T_{eff} and $\log g$, respectively. For the metallicity, we approximated the observed values for NGC 6822 ($Z = 0.3 Z_{\odot}$; Patrick et al. 2015), IC 10 ($Z = 0.3 Z_{\odot}$; Polles et al. 2019) and IC 1613 ($Z = 0.2 Z_{\odot}$; Bresolin et al. 2007) to the closest metallicity of our model grid ($\log(Z/Z_{\odot}) = -0.5$ dex). We modeled T_{eff} , $\log g$, the color excess $E(B - V)$, and the radial velocity of the system v_{rad} as free parameters. We fixed Z to break its degeneracy with the T_{eff} when using the TiO bands.

Each model was down-sampled to match the resolving power of the data: $R \sim 800$ for the MOS data and $R \sim 1000$ for the long-slit spectra. Similar to de Wit et al. (2023), we first fitted the Ca II triplet to constrain $\log g$ separately from the other parameters. The inclusion of the $\log g$ in the main fit, containing all regions of the spectrum, tends to overestimate its value. We then fixed the $\log g$ when fitting the TiO bands for T_{eff} and the spectral slope for $E(B - V)$. Lastly, we obtained v_{rad} from a cross-correlation of the model to the spectrum.

To fit the models to each star, we used ULTRANEST (Buchner 2021), a Bayesian nested sampling approach (Skilling 2004) to establish the maximum likelihood model for each star. For each parameter, we assume a flat prior. ULTRANEST then computes the posterior distributions for each free parameter (T_{eff} , $\log g$, v_{rad} , and $E(B - V)$) and finds physical correlations between each parameter pair. Specifically for T_{eff} , ULTRANEST obtained unrealistically low uncertainties; therefore, we adopted a minimal uncertainty of 50 K.

4.4. Modeled properties

Table 4 presents the best-fit properties of the 30 RSG spectra. Figure 6 shows an example fit for NGC 6822-66, a dusty P1 target classified as M0–M2 I. The top panel shows the quality of the best-fit MARCS model to our spectrum, illustrating the reliability of the derived extinction coefficients and effective temperature. The bottom panel zooms in on the Ca II triplet, showing the reliability of the derived surface gravity and radial velocity. Figure E.1 shows the other fitted spectra.

Stars with fitting problems were assigned one of four flags (see the third column of Table 4). Two spectra cannot be reproduced by the MARCS models (flag = 1) either because the TiO bands were too extreme (NGC 6822-52) or because we obtained an unreliable fit by eye (IC 10-66828). Several stars have a weaker Ca II triplet, either due to a strong TiO band hiding the strength of the absorption line ($T_{\text{eff}} \lesssim 3400$ K), or because their envelopes have not yet fully expanded, assuming that these are indeed RSGs. These then yielded values of $\log g$ near the upper limit

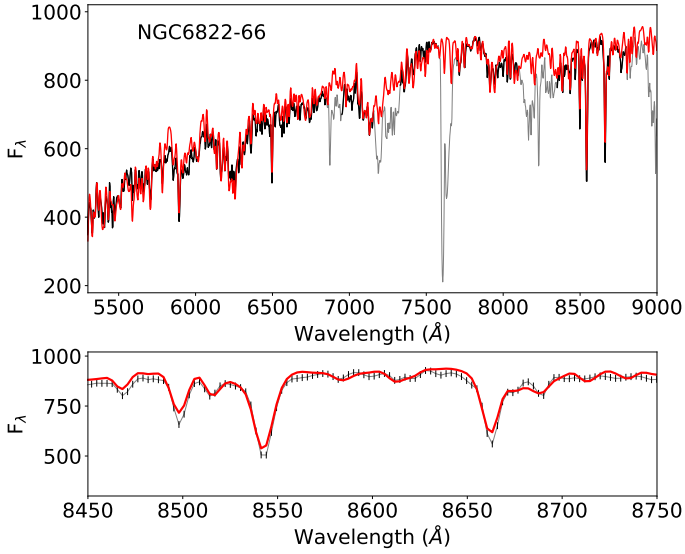


Fig. 6. MARCS model (red) fitted to the spectrum of NGC 6822-66 (black). Gray regions are excluded from the fit due to contamination by telluric absorption. F_λ is in units of $10^{-18} \text{ erg cm}^{-2} \text{ s}^{-1} \text{ Å}^{-1}$. *Top*: overall OSIRIS spectrum. *Bottom*: zoom in on the Ca II triplet.

of the grid at $\log g = 1.0$. Therefore, only the lower limits of their respective surface gravities could be derived (flag = 2). Some RSGs show TiO bands in minor disagreement with the MARCS models, yielding trustworthy results (flag = 3). Finally, some spectra had bad Ca II triplet fits, yielding unreliable values for the surface gravity (flag = 4). Uncertain classifications with high surface gravities may be reclassified in the future as oxygen-rich AGB contaminants. Finally, IC10-R3 may be a foreground star, given that such a high S/N (the highest in our RSG sample) is not expected for a low-luminosity RSG.

MOS spectra suffered from wavelength calibration issues due to a reduced wavelength range for slits near the edges and the rotator angle, which can induce shifts and therefore systematic errors up to 60 km s^{-1} . Due to this, the spread in radial velocities of sources in IC 10 is large, while for the long-slit spectra, the spread is more realistic. This issue explains the v_{rad} difference between the MOS and long-slit observations of IC10-5660 and IC10-9165.

Following de Wit et al. (2024), we computed the stellar radius and reported it in the last column of Table 4. Figure 7 compares the luminosity and radius for the present sample with the results from de Wit et al. (2024). The figure includes WOH G64 (Ohnaka et al. 2008; Levesque et al. 2009), the largest, most dusty RSG known in the Local Group, with a mass-loss rate of $\sim 10^{-4} M_\odot \text{ yr}^{-1}$, before its transition to a yellow hypergiant (Munoz-Sanchez et al. 2024b). The smallest source (IC1613-28306) was classified as a GK supergiant, possibly indicating a star at the beginning of the RSG phase.

5. Discussion

The fraction of evolved massive stars among the classified P1 and P2 targets is 67% and 60%, respectively, confirming the success of our priority system. The fractions decrease down to 37% for P5 and 17% for random targets. In particular, the P5 class suffered from extra contamination of five carbon stars and an H II region in the NGC 6822 sample. We could have avoided this by using the newest distance available for this galaxy

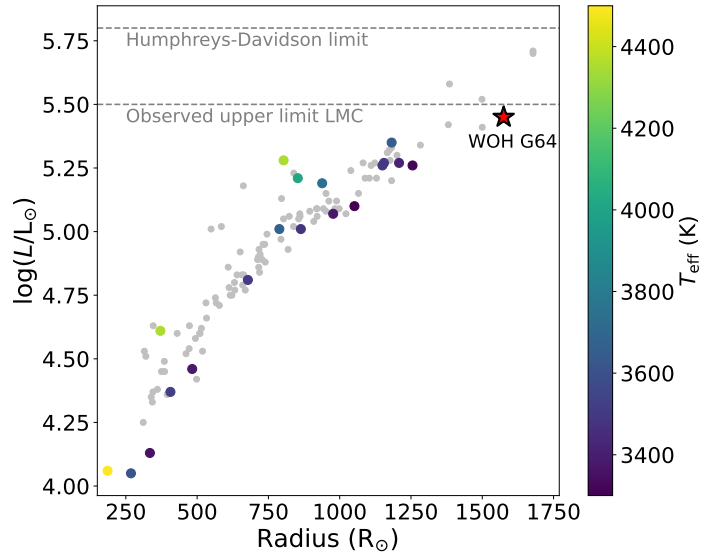


Fig. 7. Radius vs. luminosity of the RSGs in the sample. Gray sources are from the ASSESS southern sample (de Wit et al. 2024). The color indicates the effective temperature. The extreme WOH G64 in its RSG state is shown as a reference.

($0.45 \pm 0.01 \text{ Mpc}$, Zgirski et al. 2021). All priority-selected RSGs were P1, P2, or P5. Finally, H II regions were found to contaminate the P1 and P5 targets (as in Bonanos et al. 2024).

5.1. Evolutionary diagrams

To compare the obtained properties to model predictions, we constructed Hertzsprung-Russell (HR) diagrams. We computed evolutionary tracks at $Z \sim 0.2 Z_\odot$ using the grid of POSYDON models (Fragos et al. 2023; Andrews et al. 2024) to match the metallicities of the RSGs in the sample. Following de Wit et al. (2024), we assumed an exponential convective core overshoot, stellar winds that follow the “Dutch” recipe (de Jager et al. 1988; Vink et al. 2001), a mixing length fixed at $\alpha_{\text{MLT}} = 1.93$, and no stellar rotation. The tracks evolve until the end of carbon-core burning.

Figure 8 compares the positions of the 17 RSGs for which we derived their luminosity to four illustrative tracks and to the RSGs in NGC 55 from de Wit et al. (2024). The top panel shows T_{eff} based on TiO-band fits. We included IC10-5660 and IC10-9165 twice since we measured their temperature from two spectral epochs. Most sources occupy the forbidden zone, the cool region to which the evolutionary tracks do not extend. This result has been reproduced by many studies (e.g., Davies et al. 2013; de Wit et al. 2024) and is thought to be connected to the mass loss of RSGs affecting the optical temperature diagnostics (Davies & Plez 2021). Moreover, if the metallicity of the RSGs differs significantly from the default assumed value for each galaxy, $T_{\text{eff,TiO}}$ is affected. However, this cannot explain the systematic discrepancies, given that the effect of metallicity is symmetric (i.e., shifting temperatures to both slightly lower and higher values).

We then applied the scaling relations from de Wit et al. (2024) to ten RSGs to scale the $T_{\text{eff,TiO}}$ up to more representative values. The remainder of the RSGs were dropped after this point, as the relations can only be applied to RSGs in the range 3450–3950 K. We show the *i*-band-scaled temperatures and *J*-band-scaled temperatures in the middle and bottom panels of Fig. 8, respectively. In contrast to de Wit et al. (2024), the

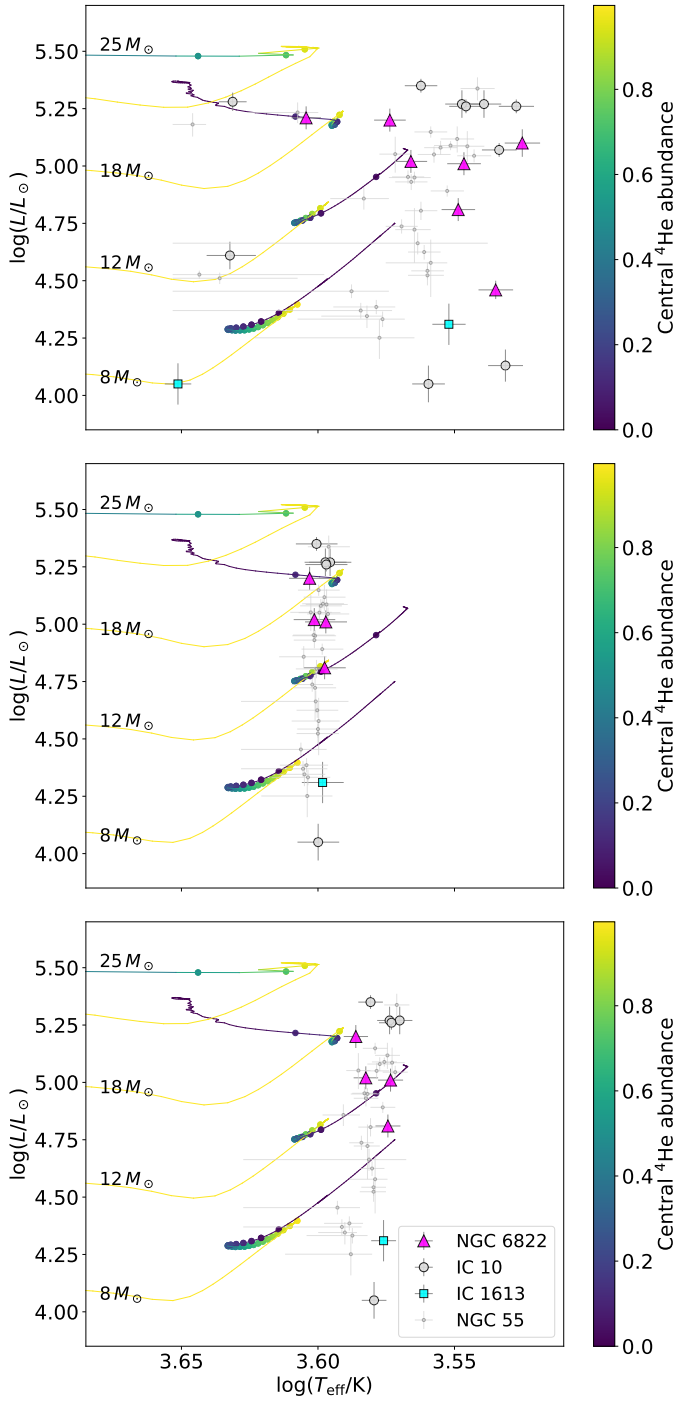


Fig. 8. HR diagram of RSGs in NGC 6822, IC 10, and IC 1613 compared to RSGs in NGC 55 (de Wit et al. 2024). Four POSYDON evolutionary tracks for $Z/Z_{\odot} = 0.2$ are overplotted; the color indicates the central helium abundance, while dots indicate intervals of 10,000 yr. Each panel includes effective temperatures determined using the following methods: TiO-band fits (*top*), the *i*-band scaling relation applied to our TiO temperatures (*middle*), and the *J*-band scaling relation (*bottom*).

hotter *J*-band-scaled temperatures align better with the evolutionary predictions, strengthening the argued use of the *J*-band diagnostics to measure the effective temperature from RSG spectra. However, similar to de Wit et al. (2024), we refrain from a firm conclusion based on the evolutionary tracks alone, given the plethora of assumptions going into the POSYDON models. Christodoulou et al. (2025) have performed a *J*-band spectral

analysis for NGC 6822-55, NGC 6822-70, NGC 6822-103, and NGC 6822-175, determining more accurate temperatures of these RSGs.

Four of our low-luminosity RSGs (IC10-20296, IC10-R3, IC1613-23465, and NGC 6822-248) are too cool to reconcile with the 8 M_{\odot} track. Their low temperature cannot be explained by mass loss alone because the low-luminosity RSGs are expected to experience weak winds (e.g., Antoniadis et al. 2024). Optical photometry was not available for IC10-20296 and IC10-R3, but the large amplitude and short-timescale variability of IC1613-23465 and NGC 6822-248 differ from those of the other RSGs. Among them, only NGC 6822-248 was robustly classified as a RSG based on spectral features. RSGs and AGB stars overlap in luminosity between $4.0 < \log(L/L_{\odot}) < 4.5$, and hence, these four targets might be evolved stars with masses $< 8 M_{\odot}$. A more detailed study of these four objects is needed to determine their nature.

5.2. Dusty RSGs

Clues of episodic mass loss may lie in the circumstellar dust. We consider a RSG dusty when its IR [3.6] – [4.5] color exceeds 0.1 mag and its absolute magnitude $M_{3.6} \leq -9.0$ mag. Out of the 28 RSGs, 20 satisfy both of these criteria, 7 random targets classified as RSGs did not have mid-IR photometry, and 1 random target had blue mid-IR colors. We compared the properties of the dusty RSGs to the statistics presented by de Wit et al. (2024). They reported a median temperature of 3570 K for 27 dusty RSGs compared to a median temperature of 3630 K for 84 non-dusty RSGs. Considering the 20 known dusty RSGs in our sample (with two duplicate measurements; 22 measured effective temperatures), we found a median temperature of 3533 K, which agrees with the findings of de Wit et al. (2024). This is approximately 100 K cooler than the non-dusty RSGs. This temperature difference could be due to the effect of mass loss, which simultaneously increases the molecular absorption (lowering T_{eff}) and provides fresh dust to the circumstellar environment.

For the extinction, we used $R_V = 3.1$ to convert the $E(B - V)$ to A_V , although the real value of the total-to-selective extinction may be higher for the circumstellar environments of massive stars (e.g., Massey et al. 2005; Maíz Apellániz et al. 2014; Brands et al. 2023). Given the large foreground extinction of IC 10, we cannot reliably compare the median A_V of our sample to those presented by de Wit et al. (2024). For this comparison, we only include RSGs from NGC 6822 and IC 1613. We calculate a median extinction of this sample of 11 dusty RSGs of $A_V = 0.53$ mag, compared to the $A_V = 1.08$ mag from the previous work for dusty RSGs and $A_V = 0.46$ mag for non-dusty RSGs. Despite the conservative criteria, we still find a marginally higher median extinction than the non-dusty sample. None of the 11 RSGs passes the criteria to be considered a dust-enshrouded RSG (Beasor & Smith 2022; de Wit et al. 2024).

Lastly, de Wit et al. (2024) reported a median $\log(L/L_{\odot}) = 5.09$ for dusty RSGs and $\log(L/L_{\odot}) = 4.88$ for non-dusty RSGs. In this work, we derive $\log(L/L_{\odot}) = 5.01$ from our sample of 20 dusty RSGs. We argue that the lower luminosity is a natural result of observing nearby galaxies and, as such, the ability to probe the lower end of the luminosity distribution. Each of these medians agrees with the conclusions of de Wit et al. (2024) that dusty RSGs are, as a population, more evolved than dust-free RSGs. If dusty RSGs are more evolved, they should also be more variable. Each RSG indicated in Fig. 5, showing a high degree of variability, also shows IR excess.

For those without *Spitzer* colors, for which we are unable to determine if they are dusty RSGs, and for those without dust, only one source was classified as a potential late M-type RSG (M2-M4 I; ID: IC10-R17), whereas the other seven sources are either K or early M-types. This contrasts sharply with the sample of known dusty RSGs, which has nine late-type RSGs, around 40% of the sample. This can be explained as the TiO bands, which increase in strength with higher mass-loss rates, are used for classification. Higher mass-loss rates should, therefore, naturally lead to later-type classifications (Davies et al. 2013; Davies & Plez 2021).

5.3. Episodic mass loss

We relied on mid-IR indicators to detect massive evolved stars (Bonanos et al. 2009, 2010). In our southern survey (i.e., Bonanos et al. 2024), we discovered massive stars in transitional phases where eruptive or episodic mass loss occurs, such as luminous blue variable candidates (Maravelias et al. 2023). In this work, we report an emission line object (NGC 6822-106) that stands out as one of the brightest mid-IR sources in our sample and one of the faintest in the optical (Fig. 2). Its extreme $G-[3.6]$ color (7.5 mag) closely resembles that of WOH G64 ($G-[3.6] = 9.2$ mag), the most extreme RSG in the Large Magellanic Cloud, which recently transitioned into a yellow hypergiant (Munoz-Sanchez et al. 2024b). NGC 6822-106 has a redder color than Var A ($G - [3.6] = 5.0$ mag), which is a yellow hypergiant from M33 that underwent an eruption for over 35 years (Hubble & Sandage 1953; Humphreys et al. 2006). The significant reddening and the strong Ca II triplet emission suggest that NGC 6822-106 is undergoing substantial mass loss, making it a compelling target for future studies. Its optical faintness prevented us from constructing a light curve and analyzing the potential eruption.

Several studies have reported spectral-type variations in RSGs (e.g., Levesque et al. 2007; Dorda et al. 2016) that are directly connected to changes in TiO strength. These variations can arise through different mechanisms. The rise and fall of convective cells at the stellar surface alter both the brightness and TiO absorption features of RSGs, creating hysteresis loops (Kravchenko et al. 2019, 2021). Episodic mass ejections can also significantly impact the spectral type and photometric variability (e.g., Massey et al. 2007; Humphreys et al. 2021; Dupree et al. 2022; Anugu et al. 2023; Munoz-Sanchez et al. 2024a). Consequently, long-term light curves are essential for identifying disruptive events associated with episodic mass loss and disentangling them from convection effects.

Two of our sources, IC10-5660 and IC10-9165, exhibit spectral variability between our two epochs. Both are luminous ($\log(L/L_{\odot}) > 5.2$), dusty RSGs that shifted from a late to an early M type over a span of two years. The *Gaia* variability of IC10-9165 prior to our observations, along with the higher extinction observed in the second epoch, suggest a mass ejection event near our first epoch. However, due to the lack of photometric coverage during our observations, we cannot confirm it. In contrast, IC10-5660 maintains constant brightness and extinction between epochs, making its spectral change more puzzling and without a clear cause.

We also classified four dusty RSGs as K-type supergiants: IC1613-28306, NGC 6822-55, IC10-5545, and IC10-26089. For the targets in IC 10, we investigated whether the high foreground extinction could explain their reddened *Spitzer* colors. Assuming a foreground extinction of $A_V = 4.3$ mag (Schlafly & Finkbeiner 2011), we estimate that foreground dust contributes

approximately $[3.6]-[4.5] \sim 0.05$ mag. After correcting for this factor, a significant IR excess remains, confirming these objects as genuinely dusty K-type RSGs. Following the recipe from Antoniadis et al. (2024, 2025), we estimated their mass-loss rate to be $\dot{M} < 10^{-7} M_{\odot} \text{yr}^{-1}$. These low rates imply an eruptive mass-loss mechanism is causing enhanced dust production (e.g., Beasor et al. 2020; Decin et al. 2024). Their light curves do not show strong variability, indicating that they are currently in a stable state. However, the mid-IR photometry was taken 20 years before our observations. Due to the absence of photometric coverage from that period, we can only speculate that a mass ejection event may have occurred back then. A possible explanation for the GK I supergiant IC1613-28306 is episodic mass loss during its approach to the Hayashi limit from the YSG phase (Cheng et al. 2024), forming dust around the supergiant.

6. Summary

The ASSESS project (Bonanos et al. 2024) investigated the role of episodic mass loss in evolved massive stars. As part of this project, we have presented a new sample of observed, evolved massive stars from our northern survey, which contains three low-metallicity galaxies: NGC 6822, IC 10, and IC 1613. We collected the photometry of 163 observed targets, obtained their spectra through multi-object and long-slit spectroscopy using GTC-OSIRIS, and spectroscopically classified 124 of the 163 spectra (122 unique objects). The majority show an IR excess in their *Spitzer* photometry. Among these, we confirmed two SNR candidates and two H II regions and found thirty-three evolved massive stars: twenty-eight RSGs, two BSGs, one YSG, one Wolf-Rayet star, and one emission-line object. Remarkably, the Ca II triplet emission and the obscuration of the emission-line object suggest an ongoing period of enhanced mass loss. All but seven of the RSGs and the Wolf-Rayet star are newly discovered evolved massive stars. This work increases the sample of RSGs in IC 10 from 1 to 17.

We derived luminosities for 17 RSGs through SED fitting and the temperatures for 28 RSGs using the MARCS radiative transfer models, contributing significantly to our knowledge of the known low-metallicity RSGs in northern galaxies. The properties of the dusty RSGs agree well with those determined by de Wit et al. (2024), with a median temperature of 3530 K and a median luminosity of $\log(L/L_{\odot}) = 5.01$. The optical spectra of two of the RSGs varied over two years, changing by a few spectral types. In particular, we find more extinction in the second epoch of IC10-9165, which suggests an episodic mass loss event. Lastly, we find four K-type RSGs with IR excess, reinforcing previous results by de Wit et al. (2024). We speculate that these four RSGs experienced episodic mass loss, leading to excessive dust formation and giving rise to the IR excess we observe.

Future studies can utilize photometry to optimize the process of finding and characterizing RSGs, specifically those with high mass loss that is potentially episodic. Using large surveys like ZTF, LSST, and NEOWISE, machine-learning algorithms such as those presented by Maravelias et al. (2022, 2025) can automatically predict the general spectral classes of the sources based on their colors and photometric variability. A combination of such algorithms can be used in low-risk, systematic large-scale studies of RSG populations in a variety of metallicity environments. Mapping the luminosities and temperatures of RSG populations can lead to the determination of the luminosity functions of RSGs in galaxies, providing an

indirect measurement of a time-averaged mass-loss rate of the RSG phase (Massey et al. 2023; Zapartas et al. 2025).

Data availability

The full Table 3 is available at the CDS via anonymous ftp to cdsarc.cds.unistra.fr (130.79.128.5) or via <https://cdsarc.cds.unistra.fr/viz-bin/cat/J/A+A/698/A279>

Acknowledgements. The authors acknowledge funding support from the European Research Council (ERC) under the European Union's Horizon 2020 research and innovation program (ASSESS; Grant agreement No. 772086). We thank Emmanouil Zapartas and the POSYDON team for providing POSYDON evolutionary tracks prior to publication. Based on observations made with the Gran Telescopio Canarias (GTC), installed at the Spanish Observatorio del Roque de los Muchachos of the Instituto de Astrofísica de Canarias, on the island of La Palma. This work is based on data obtained with the instrument OSIRIS, built by a Consortium led by the Instituto de Astrofísica de Canarias in collaboration with the Instituto de Astronomía de la Universidad Autónoma de México. OSIRIS was funded by GRANTECAN and the National Plan of Astronomy and Astrophysics of the Spanish Government. The Digitized Sky Surveys were produced at the Space Telescope Science Institute under U.S. Government grant NAG W-2166. The images of these surveys are based on photographic data obtained using the Oschin Schmidt Telescope on Palomar Mountain and the UK Schmidt Telescope. The plates were processed into the present compressed digital form with the permission of these institutions. This research made use of Astropy, a community-developed core Python package for Astronomy (Astropy Collaboration 2013, 2018) and Photutils, an Astropy package for the detection and photometry of astronomical sources (Bradley et al. 2022). "This research has made use of the VizieR catalogue access tool, CDS, Strasbourg, France (10.26093/cds/vizier). The original description of the VizieR service was published in Ochsenbein et al. (2000).

References

- Andrews, J. J., Bavera, S. S., Briel, M., et al. 2024, AAS J., submitted, [arXiv:2411.02376]
- Antoniadis, K., Bonanos, A. Z., de Wit, S., et al. 2024, *A&A*, 686, A88
- Antoniadis, K., Zapartas, E., Bonanos, A. Z., et al. 2025, *A&A*, submitted [arXiv:2503.05876]
- Anugu, N., Baron, F., Gies, D. R., et al. 2023, *AJ*, 166, 78
- Arroyo-Torres, B., Wittkowski, M., Chiavassa, A., et al. 2015, *A&A*, 575, A50
- Astropy Collaboration (Robitaille, T. P., et al.) 2013, *A&A*, 558, A33
- Astropy Collaboration (Price-Whelan, A. M., et al.) 2018, *AJ*, 156, 123
- Beasor, E. R., & Smith, N. 2022, *ApJ*, 933, 41
- Beasor, E. R., Davies, B., Smith, N., et al. 2020, *MNRAS*, 492, 5994
- Bellm, E. C., Kulkarni, S. R., Graham, M. J., et al. 2019, *PASP*, 131, 018002
- Bergemann, M., Hoppe, R., Semenova, E., et al. 2021, *MNRAS*, 508, 2236
- Bonanos, A. Z., Massa, D. L., Sewilo, M., et al. 2009, *AJ*, 138, 1003
- Bonanos, A. Z., Lennon, D. J., Köhlinger, F., et al. 2010, *AJ*, 140, 416
- Bonanos, A. Z., Tramper, F., de Wit, S., et al. 2024, *A&A*, 686, A77
- Boyer, M. L., McQuinn, K. B. W., Barmby, P., et al. 2015, *ApJS*, 216, 10
- Bradley, L., Sipőcz, B., Robitaille, T., et al. 2022, *astropy/photutils*: 1.5.0
- Brands, S. A., de Koter, A., Bestenlehner, J. M., et al. 2023, *A&A*, 673, A132
- Bresolin, F., Urbaneja, M. A., Gieren, W., Pietrzyński, G., & Kudritzki, R.-P. 2007, *ApJ*, 671, 2028
- Britavskiy, N. E., Bonanos, A. Z., Mehner, A., et al. 2015, *A&A*, 584, A33
- Britavskiy, N. E., Bonanos, A. Z., Herrero, A., et al. 2019, *A&A*, 631, A95
- Buchner, J. 2021, *J. Open Source Softw.*, 6, 3001
- Castor, J. I., Abbott, D. C., & Klein, R. I. 1975, *ApJ*, 195, 157
- Cepa, J., Aguiar, M., Escalera, V. G., et al. 2000, *SPIE Conf. Ser.*, 4008, 623
- Cepa, J., Aguiar-Gonzalez, M., Bland-Hawthorn, J., et al. 2003, *SPIE Conf. Ser.*, 4841, 1739
- Chambers, K. C., Magnier, E. A., Metcalfe, N., et al. 2016, arXiv e-prints [arXiv:1612.05560]
- Cheng, S. J., Goldberg, J. A., Cantiello, M., et al. 2024, *ApJ*, 974, 270
- Christodoulou, E., de Wit, S., Bonanos, A. Z., et al. 2025, *A&A*, submitted
- Chun, S.-H., Yoon, S.-C., Oh, H., Park, B.-G., & Hwang, N. 2022, *ApJ*, 939, 28
- Cohen, D. H., Wollman, E. E., Leutenegger, M. A., et al. 2014, *MNRAS*, 439, 908
- Cosens, M., Wright, S. A., Sandstrom, K., et al. 2024, *AJ*, 168, 250
- Crowther, P. A., Drissen, L., Abbott, J. B., Royer, P., & Smartt, S. J. 2003, *A&A*, 404, 483
- Davies, B., & Plez, B. 2021, *MNRAS*, 508, 5757
- Davies, B., Kudritzki, R.-P., Plez, B., et al. 2013, *ApJ*, 767, 3
- Davies, B., Crowther, P. A., & Beasor, E. R. 2018, *MNRAS*, 478, 3138
- de Jager, C., Nieuwenhuijzen, H., & van der Hucht, K. A. 1988, *A&AS*, 72, 259
- de Wit, S., Bonanos, A. Z., Tramper, F., et al. 2023, *A&A*, 669, A86
- de Wit, S., Bonanos, A. Z., Antoniadis, K., et al. 2024, *A&A*, 689, A46
- Decin, L., Richards, A. M. S., Marchant, P., & Sana, H. 2024, *A&A*, 681, A17
- Dorda, R., González-Fernández, C., & Negueruela, I. 2016, *A&A*, 595, A105
- Drevon, J., Millour, F., Cruzalèbes, P., et al. 2024, *MNRAS*, 527, L88
- Dupree, A. K., Strassmeier, K. G., Calderwood, T., et al. 2022, *ApJ*, 936, 18
- Dye, S., Lawrence, A., Read, M. A., et al. 2018, *MNRAS*, 473, 5113
- Elias, J. H., Frogel, J. A., & Humphreys, R. M. 1985, *ApJS*, 57, 91
- Fazio, G. G., Hora, J. L., Allen, L. E., et al. 2004, *ApJS*, 154, 10
- Förster, F., Moriya, T. J., Maureira, J. C., et al. 2018, *Nat. Astron.*, 2, 808
- Fragos, T., Andrews, J. J., Bavera, S. S., et al. 2023, *ApJS*, 264, 45
- Fullerton, A. W., Massa, D. L., & Prinja, R. K. 2006, *ApJ*, 637, 1025
- Gaia Collaboration (Prusti, T., et al.) 2016, *A&A*, 595, A1
- Gaia Collaboration (Brown, A. G. A., et al.) 2018, *A&A*, 616, A1
- Gaia Collaboration (Vallenari, A., et al.) 2023, *A&A*, 674, A1
- Gal-Yam, A. 2012, *Science*, 337, 927
- Gal-Yam, A. 2019, *ARA&A*, 57, 305
- Górski, M., Pietrzyński, G., & Gieren, W. 2011, *AJ*, 141, 194
- Groenewegen, M. A. T., & Sloan, G. C. 2018, *A&A*, 609, A114
- Gustafsson, B., Edvardsson, B., Eriksson, K., et al. 2008, *A&A*, 486, 951
- Gvaramadze, V. V., Kniazev, A. Y., & Fabrika, S. 2010, *MNRAS*, 405, 1047
- Gómez-González, V. M. A., Mayya, Y. D., & Rosa-González, D. 2016, *MNRAS*, 460, 1555
- Hubble, E., & Sandage, A. 1953, *ApJ*, 118, 353
- Hubble, E. P. 1925, *ApJ*, 62, 409
- Humphreys, R. M., Jones, T. J., Polonski, E., et al. 2006, *AJ*, 131, 2105
- Humphreys, R. M., Davidson, K., Richards, A. M. S., et al. 2021, *AJ*, 161, 98
- Humphreys, R. M., Jones, T. J., & Martin, J. C. 2023, *AJ*, 166, 50
- Irwin, M. J. 2013, in *Astrophysics and Space Science Proceedings*, 37, Thirty Years of Astronomical Discovery with UKIRT, 229
- Josselin, E., & Plez, B. 2007, *A&A*, 469, 671
- Kacharov, N., Rejkuba, M., & Cioni, M. R. L. 2012, *A&A*, 537, A108
- Kee, N. D., Sundqvist, J. O., Decin, L., de Koter, A., & Sana, H. 2021, *A&A*, 646, A180
- Khan, R., Stanek, K. Z., Kochanek, C. S., & Sonneborn, G. 2015, *ApJS*, 219, 42
- Kinman, T. D., Green, J. R., & Mahaffey, C. T. 1979, *PASP*, 91, 749
- Kopsacheili, M., Zezas, A., & Leonidaki, I. 2020, *MNRAS*, 491, 889
- Koumpia, E., Oudmaijer, R. D., Graham, V., et al. 2020, *A&A*, 635, A183
- Kravchenko, K., Chiavassa, A., Van Eck, S., et al. 2019, *A&A*, 632, A28
- Kravchenko, K., Jorissen, A., Van Eck, S., et al. 2021, *A&A*, 650, L17
- Lee, H., Grebel, E. K., & Hodge, P. W. 2003, *A&A*, 401, 141
- Levesque, E. M., & Massey, P. 2012, *AJ*, 144, 2
- Levesque, E. M., Massey, P., Olsen, K. A. G., & Plez, B. 2007, *ApJ*, 667, 202
- Levesque, E. M., Massey, P., Plez, B., & Olsen, K. A. G. 2009, *AJ*, 137, 4744
- Ma, J.-Z., Chiavassa, A., de Mink, S. E., et al. 2024, *ApJ*, 962, L36
- Maíz Apellániz, J., Evans, C. J., Barbá, R. H., et al. 2014, *A&A*, 564, A63
- Maravelias, G., Bonanos, A. Z., Tramper, F., et al. 2022, *A&A*, 666, A122
- Maravelias, G., de Wit, S., Bonanos, A. Z., et al. 2023, *Galaxies*, 11, 79
- Maravelias, G., Bonanos, A. Z., Antoniadis, K., et al. 2025, *A&A*, submitted, [arXiv:2504.01232]
- Massey, P. 1998, *ApJ*, 501, 153
- Massey, P., McNeill, R. T., Olsen, K. A. G., et al. 2007, *AJ*, 134, 2474
- Massey, P., Plez, B., Levesque, E. M., et al. 2005, *ApJ*, 634, 1286
- Mauerhan, J. C., Smith, N., Filippenko, A. V., et al. 2013, *MNRAS*, 430, 1801
- Massey, P., Neugent, K. F., Ekström, S., et al. 2023, *ApJ*, 942, 69
- McDonald, S. L. E., Davies, B., & Beasor, E. R. 2022, *MNRAS*, 510, 3132
- McMahon, R. 2012, in *Science from the Next Generation Imaging and Spectroscopic Surveys*, 37
- McQuinn, K. B. W., Boyer, M. L., Mitchell, M. B., et al. 2017, *ApJ*, 834, 78
- Montargès, M., Cannon, E., Lagadec, E., et al. 2021, *Nature*, 594, 365
- Moustakas, J., Kennicutt, Robert C., J., Tremonti, C. A., et al. 2010, *ApJS*, 190, 233
- Munoz-Sanchez, G., de Wit, S., Bonanos, A. Z., et al. 2024a, *A&A*, 690, A99
- Munoz-Sanchez, G., Kalitsounaki, M., de Wit, S., et al. 2024b, *Nat. Astron.*, submitted, [arXiv:2411.19329]
- Neill, J. D., Sullivan, M., Gal-Yam, A., et al. 2011, *ApJ*, 727, 15
- Ochsenbein, F., Bauer, P., & Marcout, J. 2000, *A&AS*, 143, 23
- Ohnaka, K., Driebe, T., Hofmann, K. H., et al. 2020, *A&A*, 484, 371
- Patrick, L. R., Evans, C. J., Davies, B., et al. 2015, *ApJ*, 803, 14
- Polles, F. L., Madden, S. C., Lebouteiller, V., et al. 2019, *A&A*, 622, A119
- Rieke, G. H., Young, E. T., Engelbracht, C. W., et al. 2004, *ApJS*, 154, 25

- Rubin, R. H., Simpson, J. P., Colgan, S. W. J., et al. 2016, [MNRAS](#), **459**, 1875
- Schlafly, E. F., & Finkbeiner, D. P. 2011, [ApJ](#), **737**, 103
- Skilling, J. 2004, in Bayesian Inference and Maximum Entropy Methods in Science and Engineering: 24th International Workshop on Bayesian Inference and Maximum Entropy Methods in Science and Engineering, eds. R. Fischer, R. Preuss, & U. V. Toussaint, [American Institute of Physics Conference Series](#), 735, 395
- Smartt, S. J. 2015, [PASA](#), **32**, e016
- Smartt, S. J., Eldridge, J. J., Crockett, R. M., & Maund, J. R. 2009, [MNRAS](#), **395**, 1409
- Smith, N. 2014, [ARA&A](#), **52**, 487
- Smith, N., Andrews, J. E., Filippenko, A. V., et al. 2022, [MNRAS](#), **515**, 71
- Solf, J. 1978, [A&AS](#), **34**, 409
- Sukhbold, T., Ertl, T., Woosley, S. E., Brown, J. M., & Janka, H. T. 2016, [ApJ](#), **821**, 38
- Telford, O. G., Chisholm, J., Sander, A. A. C., et al. 2024, [ApJ](#), **974**, 85
- Tikhonov, N. A., & Galazutdinova, O. A. 2009, [Astron. Lett.](#), **35**, 748
- Tonry, J. L., Denneau, L., Heinze, A. N., et al. 2018, [PASP](#), **130**, 064505
- Tully, R. B., Courtois, H. M., Dolphin, A. E., et al. 2013, [AJ](#), **146**, 86
- van Loon, J. T., Cioni, M. R. L., Zijlstra, A. A., & Loup, C. 2005, [A&A](#), **438**, 273
- Vink, J. S., & Sander, A. A. C. 2021, [MNRAS](#), **504**, 2051
- Vink, J. S., de Koter, A., & Lamers, H. J. G. L. M. 2000, [A&A](#), **362**, 295
- Vink, J. S., de Koter, A., & Lamers, H. J. G. L. M. 2001, [A&A](#), **369**, 574
- Yang, H., & Skillman, E. D. 1993, [AJ](#), **106**, 1448
- Yang, M., Bonanos, A. Z., Jiang, B.-W., et al. 2018, [A&A](#), **616**, A175
- Yang, M., Bonanos, A. Z., Jiang, B., et al. 2023, [A&A](#), **676**, A84
- Yoon, S.-C., & Cantiello, M. 2010, [ApJ](#), **717**, L62
- Zapartas, E., de Wit, S., Antoniadis, K., et al. 2025, [A&A](#), **697**, A167
- Zgirski, B., Pietrzyński, G., Gieren, W., et al. 2021, [ApJ](#), **916**, 19

Appendix A: Observation data

Table A.1: Distribution of targets and target priorities per galaxy.

Galaxy	P1	P2	P3	P4	P5	P6	R	Total
IC 10	2	3	6	0	39	73	–	123
<i>Field A</i>	1	2	2	0	16	16	18	55
<i>long-slit</i>	0	0	0	0	5	0	25	30
IC 1613	2	0	0	0	7	8	–	17
<i>long-slit</i>	0	0	0	0	3	0	4	7
NGC 6822	11	4	1	0	75	6	–	97
<i>Field A</i>	3	1	0	0	19	0	11	34
<i>Field B</i>	4	2	1	0	19	1	7	35
<i>long-slit</i>	1	0	0	0	1	0	0	2
Total observed	9	5	3	0	63	17	65	163
Total classified	6	5	1	0	39	8	65	124

Notes. Two sources in IC 10 (IC10-5660 and IC10-9165) were observed in both the MOS and long-slit modes.

Table A.2: OSIRIS observations.

Galaxy	Field or Target ID	R.A. (J2000)	Dec. (J2000)	UT Date ^(a)	MJD ^(b)	Mode ^(c)	T_{exp} (s)	Airmass ^(d)	Seeing ($''$)
NGC 6822	A	19:44:54.07	−14:50:36.3	29 Jun 2020	59029.17	PRE	1 × 15	1.55	1.4
NGC 6822	B	19:44:53.67	−14:44:55.1	29 Jun 2020	59029.18	PRE	1 × 15	1.57	1.3
IC 10	A	00:20:05.19	59:18:46.8	29 Jun 2020	59029.18	PRE	1 × 15	1.32	1.4
NGC 6822	A	19:44:54.07	−14:50:36.3	15 Aug 2020	59076.94	MOS	2 × 1350	1.40	0.5
NGC 6822	A	19:44:54.07	−14:50:36.3	15 Aug 2020	59076.97	MOS	2 × 1350	1.38	0.6
IC 10	A	00:20:05.19	59:18:46.8	16 Aug 2020	59077.10	MOS	2 × 1350	1.20	0.7
IC 10	A	00:20:05.19	59:18:46.8	16 Aug 2020	59077.13	MOS	2 × 1350	1.17	0.7
NGC 6822	B	19:44:53.67	−14:44:55.1	16 Aug 2020	59077.93	MOS	2 × 1350	1.41	0.8
NGC 6822	B	19:44:53.67	−14:44:55.1	16 Aug 2020	59077.96	MOS	2 × 1350	1.38	0.8
NGC 6822	106	19:45:11.69	−14:50:48.5	3 Aug 2022	59794.00	LSS	3 × 1200	1.38	0.8
IC 1613	23465	01:04:17.83	02:13:24.7	6 Aug 2022	59797.15	LSS	3 × 1000	1.19	0.9
IC 1613	d2	01:04:22.33	02:07:28.5	7 Aug 2022	59798.18	LSS	3 × 1200	1.13	0.8
IC 10	d1	00:19:33.29	59:20:30.8	19 Aug 2022	59810.97	LSS	3 × 1200	1.56	0.9
IC 10	35694	00:20:58.17	59:21:34.4	24 Aug 2022	59815.13	LSS	3 × 1200	1.16	0.9
IC 10	d2	00:19:58.81	59:19:53.9	24 Aug 2022	59815.02	LSS	3 × 1200	1.33	0.8

Notes. ^(a)UT date at the start of the observations. ^(b)MJD at the start of the OB. ^(c)PRE, MOS, and LSS correspond to the pre-imaging, multi-object spectroscopy, and long-slit modes. ^(d)Mean value of the first and last exposure (except for PRE mode).

Appendix B: Example spectra for highlighted classes

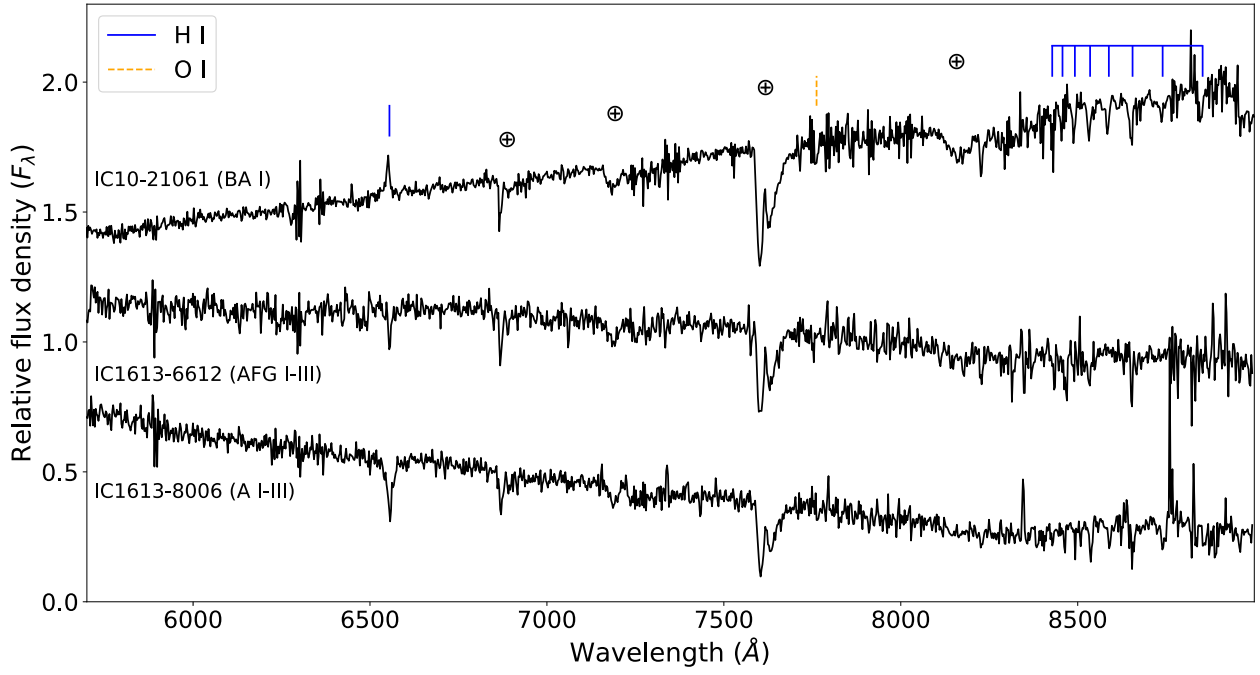


Fig. B.1: Similar to Fig. 3, but for two BSGs and one YSG. The oxygen triplet, $H\alpha$, and the Paschen series are identified.

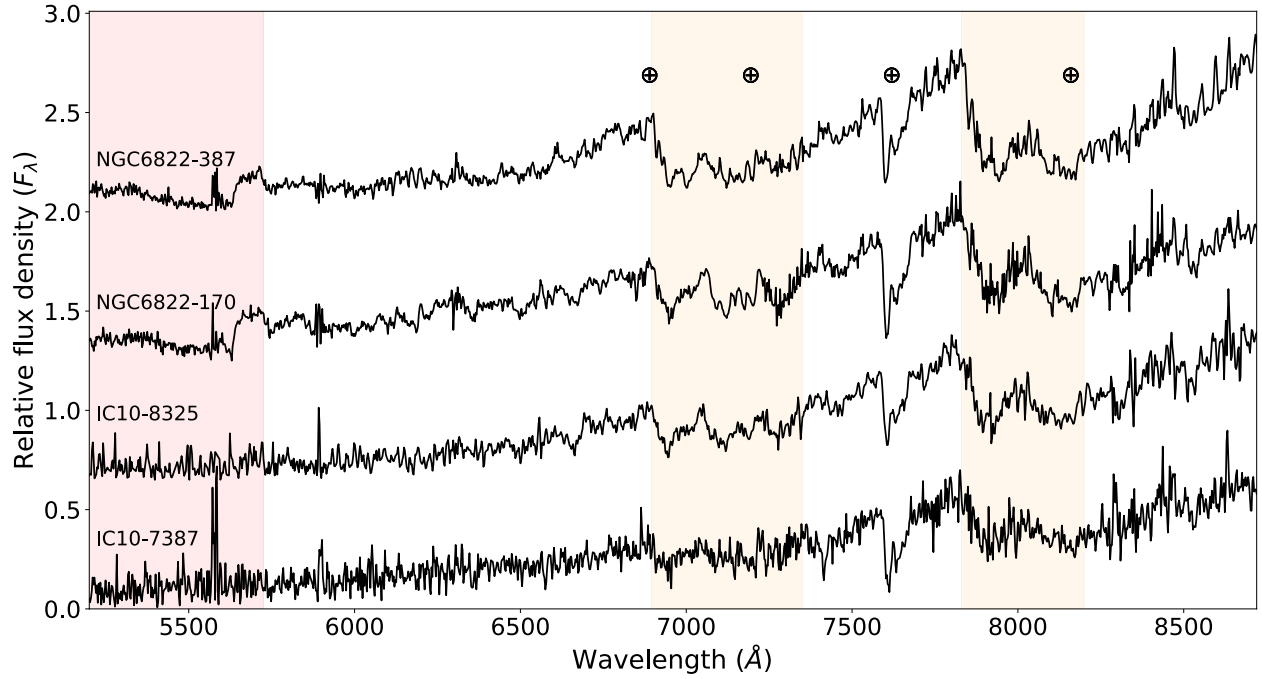


Fig. B.2: Similar to Fig. 3, but for carbon stars. Regions of significant carbon absorption are identified in orange (CN) and red (C_2 ; for NGC 6822-387 and NGC 6822-170).

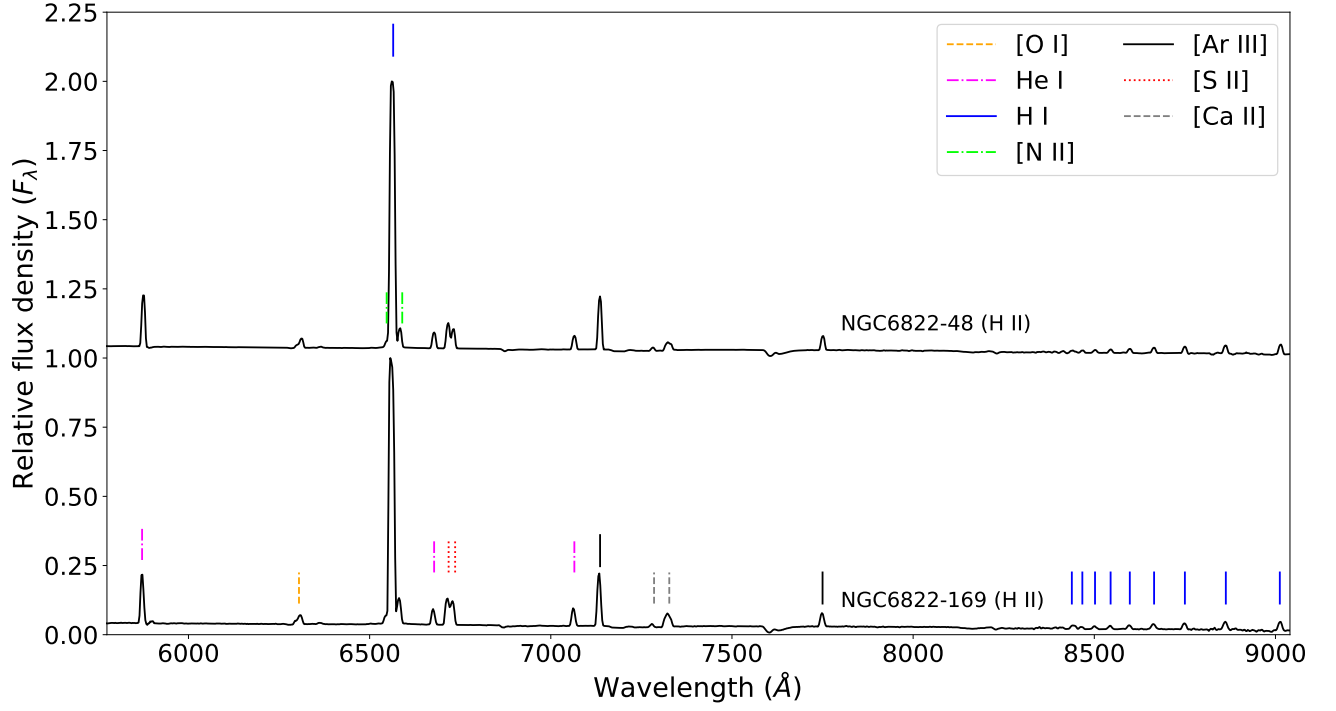


Fig. B.3: Similar to Fig. 3, but for the H II regions. Primary emission lines are identified.

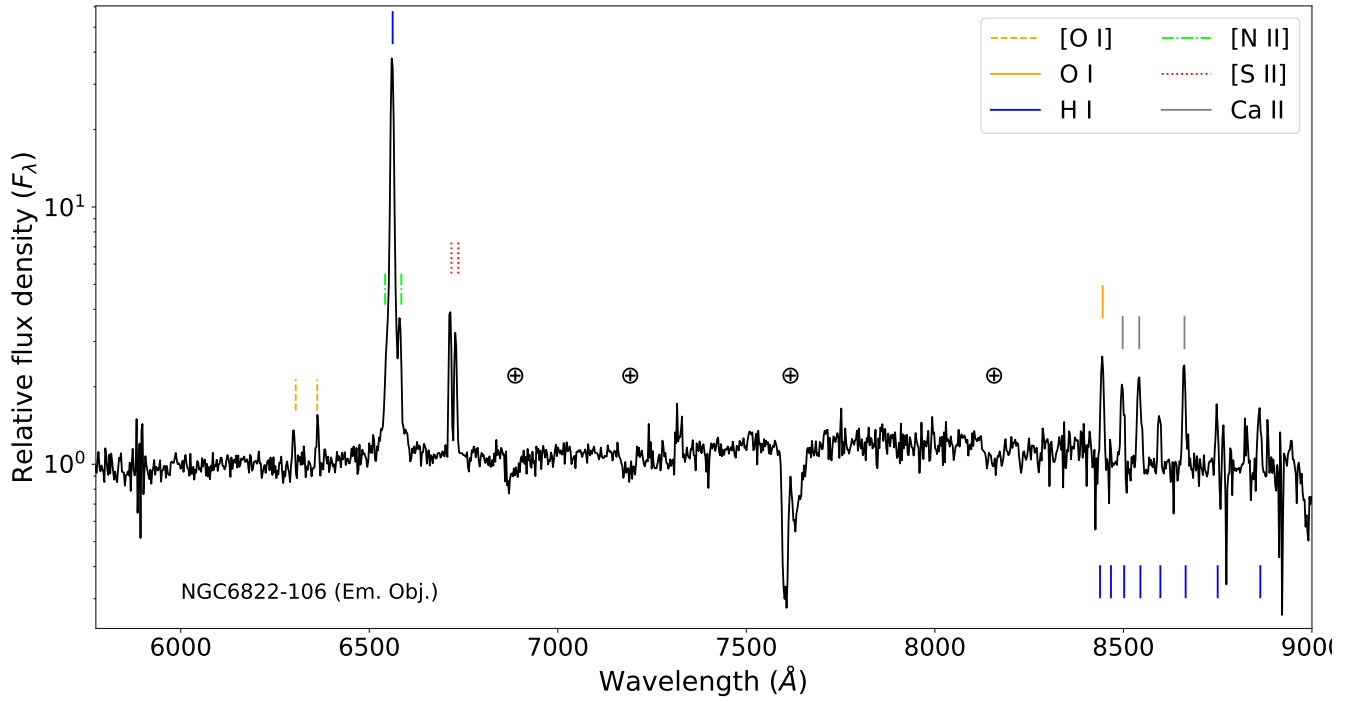


Fig. B.4: Similar to Fig. 3, but for the emission line object. Primary emission lines are identified.

Appendix C: SED fits

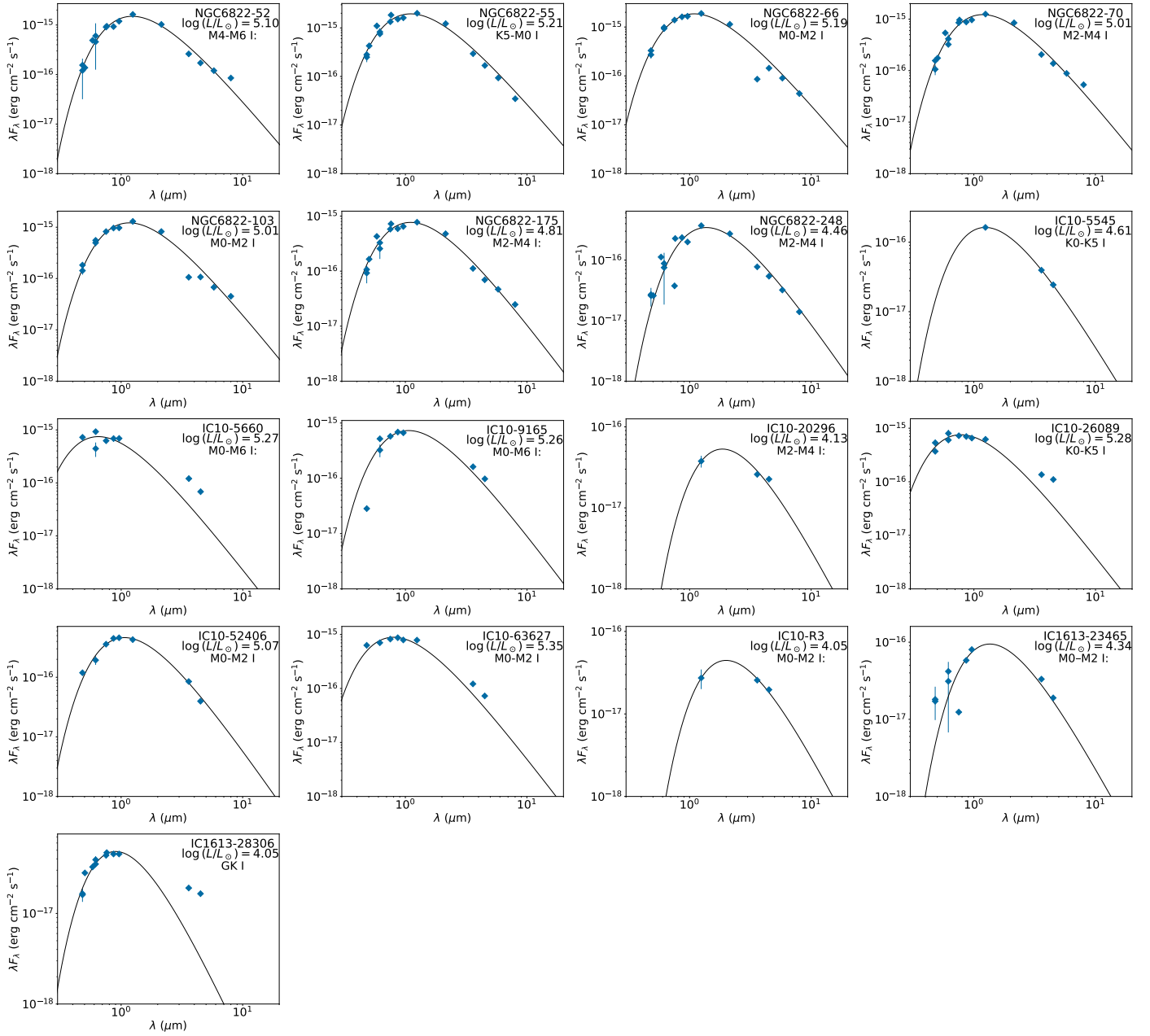


Fig. C.1: Black bodies fitted to the photometry from *Gaia*, Pan-STARRS1, VISTA, ZTF, and *Spitzer*. The target name, derived luminosity, and spectral type are indicated in each panel.

Appendix D: Light curves

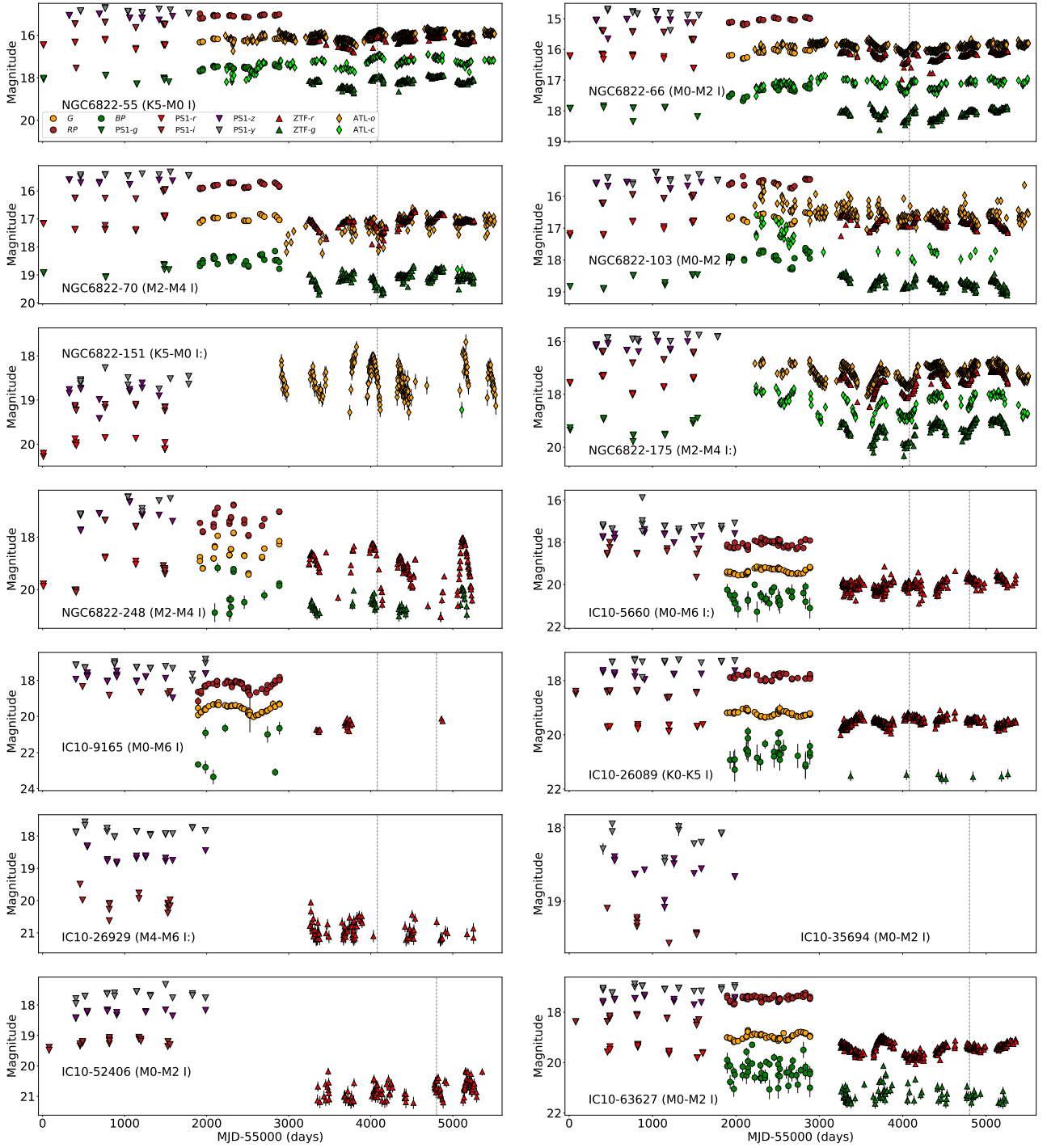


Fig. D.1: Multi-survey optical light curve of the RSGs. Apparent magnitudes from Pan-STARRS1 DR2 (triangles: *gri*), *Gaia* DR3 (circles: *G*, *BP*, *RP*), ZTF (upper triangles: *g*, *r*), and ATLAS (diamonds: *c*, *o*) are shown. The vertical dashed line indicates the epoch of the OSIRIS spectroscopy.

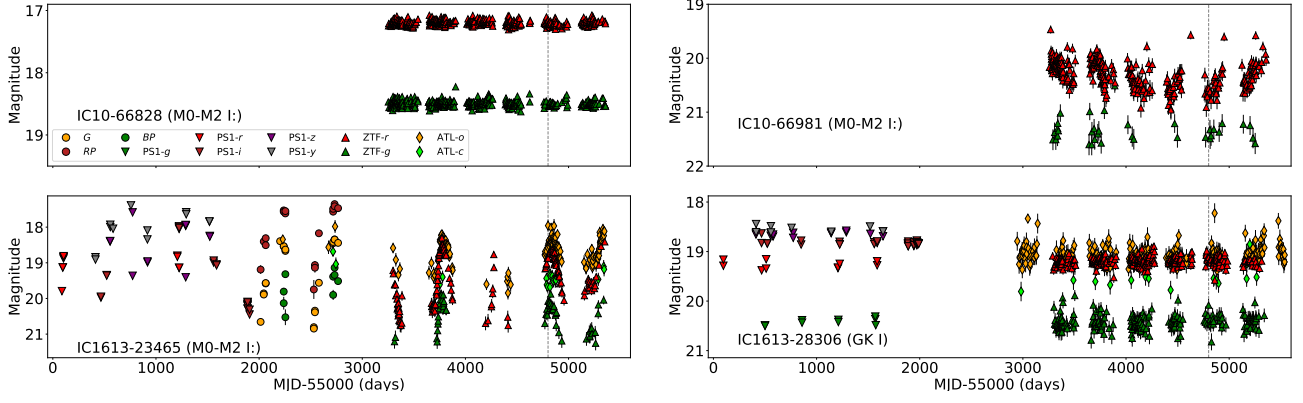


Fig. D.1: Continued.

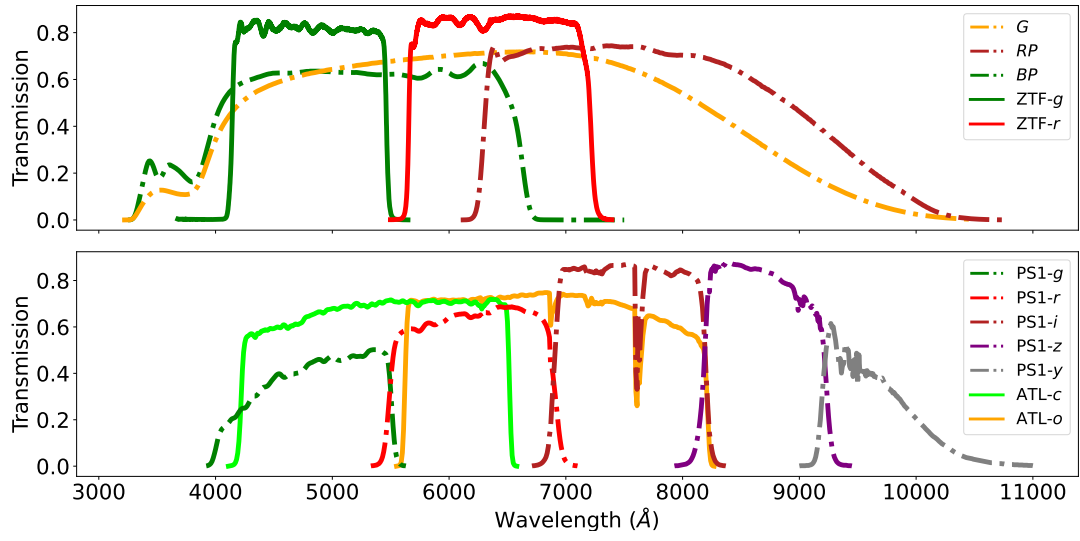


Fig. D.2: Transmission of the photometric filters used for the light curves.

Appendix E: Spectra and fitted models

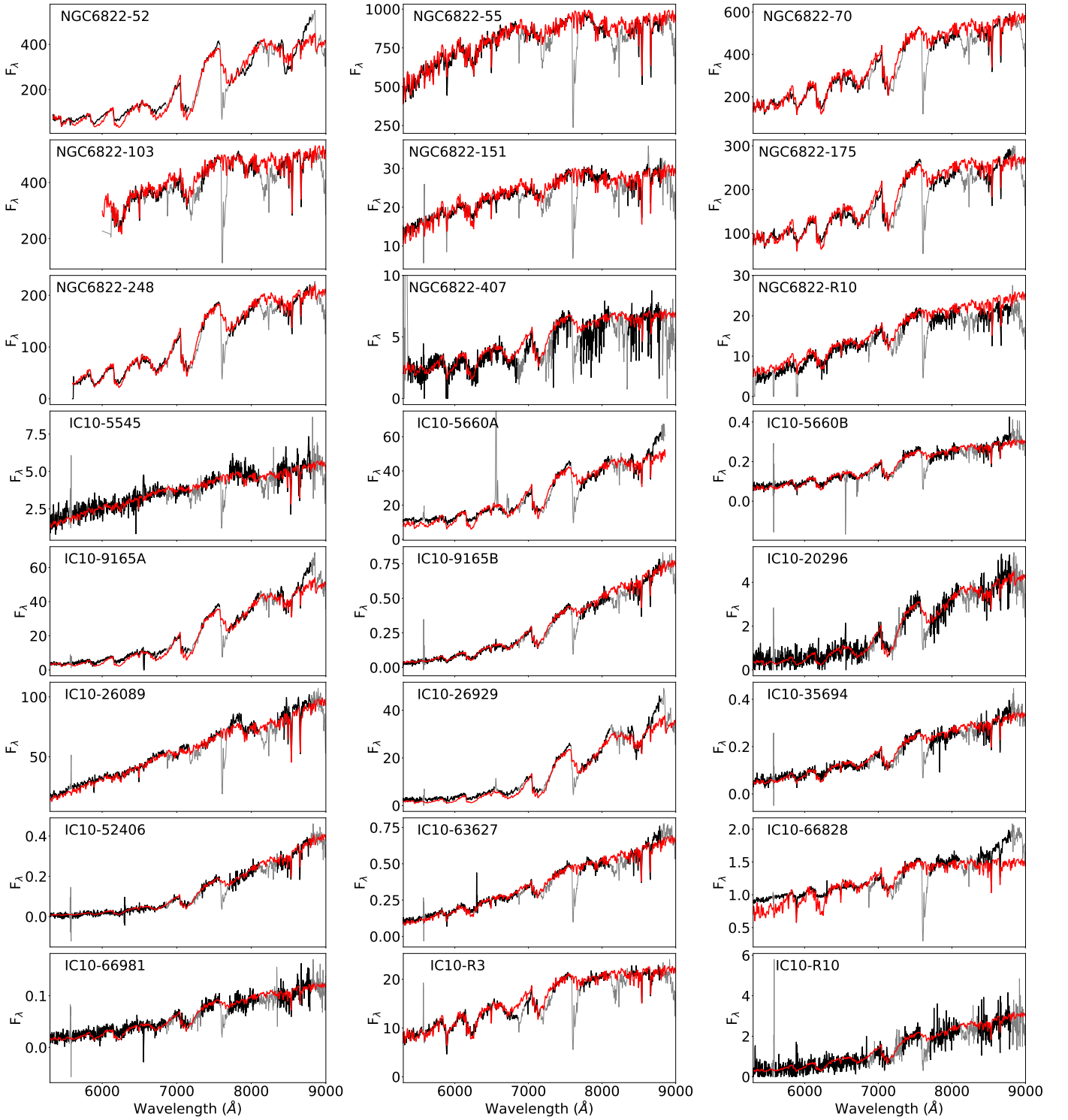


Fig. E.1: Best-fit MARCS models (red) to all spectra of RSGs (black). Gray regions are excluded from the fit due to contamination by telluric absorption. F_λ is in units of $10^{-18} \text{ erg cm}^{-2} \text{ s}^{-1} \text{ \AA}^{-1}$.

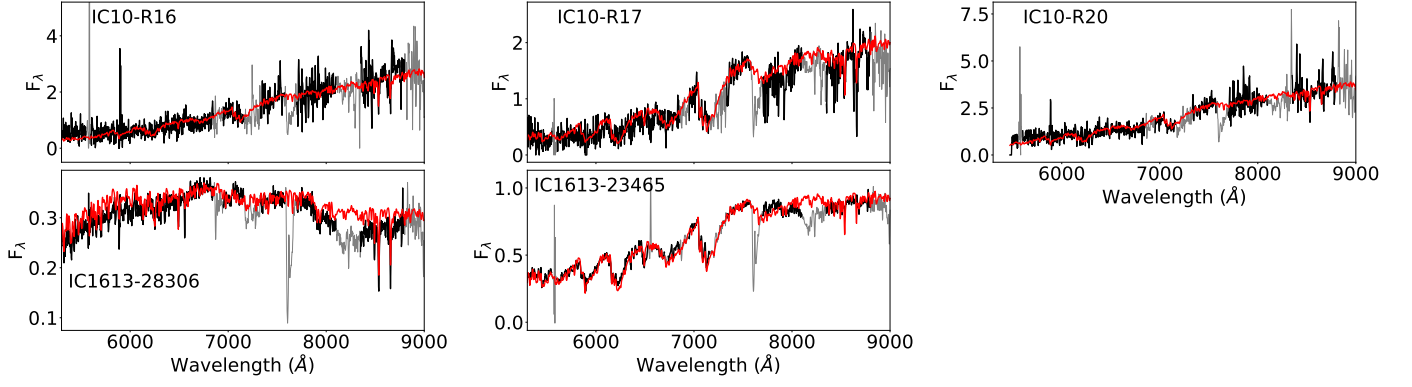


Fig. E.1: Continued.